

Lifting-based Global Optimisation over Riemannian Manifolds: Theory and Applications in Cryo-EM

Willem Diepeveen* Jan Lellmann† Ozan Öktem‡
Carola-Bibiane Schönlieb*

Abstract

We propose ellipsoidal support lifting (ESL), a lifting-based optimisation scheme for approximating the global minimiser of a smooth function over a Riemannian manifold. Under a uniqueness assumption on the minimiser we show several theoretical results, in particular an error bound with respect to the global minimiser. Additionally, we use the developed theory to integrate the lifting-based optimisation scheme into an alternating minimisation method for joint homogeneous volume reconstruction and rotation estimation in single particle cryogenic-electron microscopy (Cryo-EM), where typically tens of thousands of manifold-valued minimisation problems have to be solved. The joint recovery method arguably overcomes the typical trade-off between noise-robustness and data-consistency – while remaining computationally feasible –, and is used to test both the theoretical predictions and algorithmic performance through numerical experiments with Cryo-EM data.

1 Introduction

Variational models are commonly used in data analysis and for solving ill-posed inverse problems. In this work we are interested in variational models with smooth objectives over a Riemannian manifold, thus leading to a problem of the form

$$\inf_{p \in \mathcal{M}} F(p) \quad \text{for some smooth energy function } F: \mathcal{M} \rightarrow \mathbb{R}. \quad (1)$$

A numerical scheme for solving eq. (1) needs to account for the non-linear manifold structure of \mathcal{M} . There have been numerous efforts in developing minimisation algorithms that respects the underlying geometry of the data [1, 11, 15, 51], but many of these methods — or generally the conscious use of the intrinsic manifold-structure of the data — are by no means mainstream in applications.

An application where such manifold-valued minimisation problems arise – but where the manifold-structure is typically not leveraged – is cryogenic-electron microscopy (Cryo-EM) single particle analysis. This is a tomographic imaging technique for determining the 3D structure (map) of a biomolecule from multiple 2D transmission electron microscope (TEM) images,

*Faculty of Mathematics, University of Cambridge, Cambridge (wd292@cam.ac.uk, cbs31@cam.ac.uk).

†Institute of Mathematics and Image Computing, University of Lübeck, (lellmann@mic.uni-luebeck.de).

‡Department of Mathematics, KTH–Royal Institute of Technology (ozan@kth.se)

each representing the ‘projection’ of the biomolecule in some unknown 3D rotation ([61, Figure 1]). Joint 3D map reconstruction and rotation estimation from these 2D images is typically approached through an alternating update scheme, where recovering the unknown rotation associated with each 2D image leads to a non-convex minimisation problem of the form in eq. (1) with $\mathcal{M} = \text{SO}(3)$ [8]. Methods for addressing this that are currently used routinely in Cryo-EM labs either avoid estimating the rotation (and instead resort to marginalisation) or *do not use* the intrinsic manifold-structure of the rotation group $\text{SO}(3)$ in the optimisation.

In this work we aim to approximate solutions to problem eq. (1) and argue that leveraging the manifold-structure with our method – when applied to Cryo-EM – yields a practical algorithm without the typical trade-off between noise-robustness and data-consistency, which similar methods face.

1.1 Related work

Optimisation problems similar to eq. (1) can at least be traced back to 1972 [48], where the paradigm was to rely on Euclidean solvers while accounting for the manifold as a constraint set in \mathbb{R}^d on which each iterate had to be projected throughout the optimisation scheme. Such methods are not generally applicable since some manifolds are not defined as constraint sets in \mathbb{R}^d , as is the case with the Grassmann manifold and symmetric positive definite matrices. Also, alternatively resorting to local charts and performing the optimisation using a Euclidean solver has several drawbacks. As an example, symmetries of the manifold are poorly accounted for, distortions of the metric may corrupt convergence rates, and restricting ourselves to local neighbourhoods makes global analysis impossible [32]. These issues can be resolved by passing to *intrinsic* methods, where optimisation is formalised in terms of several structures and mappings on the manifold that do not depend on the specific embedding or chart. For this reason, the development and study of intrinsic algorithms for optimisation on manifolds has become a flourishing field, especially after seminal works in the mid-1990s [64, 68] and the area still continues to inspire new results [20].

Within the intrinsic paradigm to optimisation on manifolds one can talk about global minimisation. In the Euclidean case, convexity is key for efficiently finding a unique global minimiser of a function and having non-smoothness is no real issue for modern algorithms. For manifolds, only a certain subset allows for existence of convex functions. That is, on *Hadamard manifolds* – Riemannian manifolds that are complete, simply connected, and have non-positive sectional curvature – convexity can be generalized and has been crucial in many of the convergence proofs. Indeed, besides the standard gradient-based methods [78] a myriad of algorithms exploiting special structure of the convex function of interest have been generalized from the Euclidean case only very recently [2, 5, 9, 12, 10].

Finding a global minimiser on non-Hadamard manifolds, e.g., $\text{SO}(3)$, has shown to be more challenging as there is no notion of convexity. Particle-based methods – either stochastic [22] or deterministic [19] – have been shown to being able to find global minimisers, but might not be very suitable for large-scale applications – where scalability is key –, such as rotation estimation in alternating minimisation-based joint 3D map and rotation recovery in Cryo-EM. Lifting-based methods on the other hand – and in the case of manifolds particularly measure-based lifting methods – have shown great potential performance-wise [45, 72, 73]. However, unless there is special structure in the energy functional and optimisation is over scalars [53], the process of projecting a solution back onto the original space cannot be expected to be a minimiser of the original functional and to the best of our knowledge error bounds are unknown.

1.2 Specific contributions

The overall contribution of this paper is in the theory and algorithm development for solving minimisation problems of the form eq. (1) where the Riemannian manifold \mathcal{M} is not necessarily Hadamard. Particular emphasis is on deriving error estimates for solving such problems (global optimisation over Riemannian manifolds). Such optimisation problems arise when regularising certain challenging large-scale inverse problems with high noise, like the one in Cryo-EM. This brings us to the second part of our contribution, namely to ensure the optimisation solver is noise-robust while maintaining sufficient consistency against measured data (noise-robust and data-consistent rotation estimation in Cryo-EM).

Global optimisation over Riemannian manifolds For global optimisation over manifolds we propose ellipsoidal support lifting (ESL), a new measure-based lifting scheme which allows for an error analysis and gives ellipsoidal locality of the support of the measure around the global minimiser that can be used to construct a practical algorithm. Theoretical results are tested in numerical experiments.

Noise-robust and data-consistent rotation estimation in Cryo-EM The joint rotation estimation and recovery of the 3D map typically involves the trade-off between noise-robustness and data-consistency. Based on the theoretical framework for optimisation over manifolds that is developed, we propose a new joint recovery scheme with a lifting-based rotation estimation part that arguably takes into account both noise-robustness and data-consistency, while still being numerically feasible. Performance is tested in numerical experiments.

1.3 Outline

For the reader's convenience, the material in the paper is divided into two parts: one solely focuses on problem eq. (1) and our proposed optimisation method and the other on its application to inverse problems in Cryo-EM.

For the first part, Section 2 introduces basic notions from differential geometry, Riemannian geometry and optimal transport which then are used in measure-based lifting. In section 3 we propose a new lifting-based optimisation scheme and section 4 contains proofs of the main theoretical results.

The second part of the paper focuses on the application of lifting-based optimisation to Cryo-EM. More specifically, section 5 discusses the Cryo-EM inverse problem in more detail and elaborates on the aforementioned trade-off between noise-robustness and data-consistency through an additional Cryo-EM-specific literature review. Next, the theory and algorithms from section 3 are adapted and integrated into a joint reconstruction and rotation estimation method for single particle Cryo-EM data assuming homogeneous particles (section 6) and are argued to resolve the problems posed in section 5. Numerical results are shown in section 7 and section 8 concludes the paper with a summary and discussion of our proposed theory and method for Cryo-EM.

2 Preliminaries

The aim here is to provide essential notions from Riemannian geometry and optimal transport (section 2.1). We then introduce basic ideas underlying lifting methods for optimisation on manifolds (section 2.2).

2.1 Riemannian geometry and optimal transport

This overview is based on [14, 18, 44, 55] for differential and Riemannian geometry and on [71] for optimal transport.

Riemannian Geometry Let \mathcal{M} be a smooth manifold. Its *tangent space* at $p \in \mathcal{M}$ is denoted by $\mathcal{T}_p\mathcal{M}$ and for *tangent vectors* we write X_p or just X . Next, $\partial\mathcal{M}$ denotes its boundary (assuming it exists). Furthermore, \mathcal{M} is a *Riemannian manifold* if, at each point $p \in \mathcal{M}$, there is a smoothly varying *metric tensor* $(\cdot, \cdot)_p: \mathcal{T}_p\mathcal{M} \times \mathcal{T}_p\mathcal{M} \rightarrow \mathbb{R}$. This tensor induces a (*Riemannian*) *metric* $d_{\mathcal{M}}: \mathcal{M} \times \mathcal{M} \rightarrow \mathbb{R}_+$.

The metric tensor can also be used to construct a unique affine connection, the *Levi-Civita connection* (or *covariant derivative*) that is denoted by $\nabla_{(\cdot)}(\cdot)$. This connection is in turn the cornerstone of a myriad of manifold mappings. One is the notion of a *geodesic*, which for two points $p, q \in \mathcal{M}$ is defined as the curve $\gamma_{p,q}: [0, 1] \rightarrow \mathcal{M}$ with minimal length that connects p with q . This notion is well-defined if the manifold is *geodesically connected*, i.e., any two points $p, q \in \mathcal{M}$ can be connected with a curve that is contained in \mathcal{M} . Another closely related notion is the curve $t \mapsto \gamma_{p,X}(t)$ for a geodesic starting from $p \in \mathcal{M}$ with velocity $\dot{\gamma}_{p,X}(0) = X \in \mathcal{T}_p\mathcal{M}$. This can be used to define the *exponential map* $\exp_p: \mathcal{G}_p \rightarrow \mathcal{M}$ as

$$\exp_p(X) := \gamma_{p,X}(1) \quad \text{where } \mathcal{G}_p \subset \mathcal{T}_p\mathcal{M} \text{ is the set on which } \gamma_{p,X}(1) \text{ is defined.}$$

The manifold \mathcal{M} is said to be *complete* whenever $\mathcal{G}_p = \mathcal{T}_p\mathcal{M}$. Furthermore, the *logarithmic map* $\log_p: \exp(\mathcal{G}'_p) \rightarrow \mathcal{G}'_p$ is defined as the inverse of \exp_p , so it is well-defined on $\mathcal{G}'_p \subset \mathcal{G}_p$ where \exp_p is a diffeomorphism. Moreover, for a smooth function $F: \mathcal{M} \rightarrow \mathbb{R}$ and a point $p \in \mathcal{M}$, the metric tensor $(\cdot, \cdot)_p: \mathcal{T}_p\mathcal{M} \times \mathcal{T}_p\mathcal{M} \rightarrow \mathbb{R}$ allows to construct the *Riemannian gradient* at $p \in \mathcal{M}$ as the unique tangent vector $\text{grad}_p F \in \mathcal{T}_p\mathcal{M}$ such that

$$(\text{grad}_p F, X)_p := XF \quad \text{holds for any } X \in \mathcal{T}_p\mathcal{M}.$$

When combined with the Levi-Civita connection, we in addition can define the *Riemannian Hessian*

$$\text{Hess}_p F: \mathcal{T}_p\mathcal{M} \times \mathcal{T}_p\mathcal{M} \rightarrow \mathbb{R} \quad \text{at } p \in \mathcal{M},$$

as the unique bilinear form that satisfies

$$\text{Hess}_p F(X, Y) := (\nabla_X \text{grad}_p F, Y)_p \quad \text{for any } X, Y \in \mathcal{T}_p\mathcal{M}$$

The final two notions derived from the Riemannian metric are the eigenvalues and a determinant of a symmetric bi-linear form. These are less frequently used in general theory of Riemannian geometry, but they will be important for us.

Definition 2.1 (Eigenvalue of a bi-linear form). *Let \mathcal{M} be a Riemannian manifold and the mapping $Q: \mathcal{T}_p\mathcal{M} \times \mathcal{T}_p\mathcal{M} \rightarrow \mathbb{R}$ is a bi-linear form at some given $p \in \mathcal{M}$. We say that $\lambda \in \mathbb{R}$ is an eigenvalue of Q if there is a non-trivial tangent vector $X \in \mathcal{T}_p\mathcal{M}$ at p such that*

$$Q(X, Y) = \lambda(X, Y)_p \quad \text{for all } Y \in \mathcal{T}_p\mathcal{M}. \quad (2)$$

X is called the corresponding eigenvector of Q on $\mathcal{T}_p\mathcal{M}$.

Definition 2.2 (Determinant of a bi-linear form). *Let \mathcal{M} be a Riemannian manifold and let $Q: \mathcal{T}_p\mathcal{M} \times \mathcal{T}_p\mathcal{M} \rightarrow \mathbb{R}$ be a symmetric bi-linear form at a given $p \in \mathcal{M}$ with real eigenvalues $\lambda_1, \dots, \lambda_d$, where $d := \dim(\mathcal{M})$. We say that the determinant $\det(Q)$ of the bi-linear form Q is the product of the eigenvalues of Q , i.e.,*

$$\det(Q) := \prod_{i=1}^d \lambda_i. \quad (3)$$

Optimal transport Lifting is a key strategy for solving non-convex minimisation over some Riemannian manifold \mathcal{M} (section 2.2). The idea is to replace the minimisation over \mathcal{M} with one over probability measures on \mathcal{M} . It therefore becomes necessary to work with probability measures on \mathcal{M} and to have a metric over the space of such measures. We consider measures with finite s -th moment and use the Wasserstein distance as a metric on such measures.

Definition 2.3 (Wasserstein space and distance, [71, Def.6.4]). *Let \mathcal{M} be a connected Riemannian manifold with metric $d_{\mathcal{M}}$ and $\mathbb{P}(\mathcal{M})$ is the space of Borel probability measures over \mathcal{M} . The Wasserstein space of order $s \geq 1$ on \mathcal{M} is defined as*

$$\mathbb{P}_s(\mathcal{M}) := \left\{ \mu \in \mathbb{P}(\mathcal{M}) \mid \int_{\mathcal{M}} d_{\mathcal{M}}(p_0, p)^s d\mu(p) < +\infty, \text{ for all } p_0 \in \mathcal{M} \right\}, \quad (4)$$

and the Wasserstein- s distance is a mapping $W_s: \mathbb{P}_s(\mathcal{M}) \times \mathbb{P}_s(\mathcal{M}) \rightarrow \mathbb{R}_+$ defined as

$$W_s(\mu, \nu) := \left(\inf_{\pi \in \Gamma(\mu, \nu)} \int_{\mathcal{M} \times \mathcal{M}} d_{\mathcal{M}}(p, q)^s d\pi(p, q) \right)^{1/s}. \quad (5)$$

Here, $\Gamma(\mu, \nu) \subset \mathbb{P}(\mathcal{M} \times \mathcal{M})$ is the set of all couplings, i.e., probability measures on $\mathcal{M} \times \mathcal{M}$ with marginals μ and ν .

The Wasserstein- s distance defines a (finite) distance on $\mathbb{P}_s(\mathcal{M})$ that defines the topology in which we consider convergence of sequences of measures. It also provides the tools for constructing – and later analysing – the lifting approach to optimisation on manifolds.

2.2 Lifting methods for global optimisation on manifolds

The minimisation in eq. (1) is typically a non-convex optimisation problem, so solving it with standard techniques from convex optimisation run into the risk of getting stuck in local minima. One approach to address such non-convex manifold optimisation problems is through *lifting*, which provides – for low-dimensional manifolds – a computationally feasible convex relaxation. In case of measure-based lifting, the method consists of roughly four main steps: convexification, projection, discretisation and relaxation. The first three steps are fairly standard when lifting is phrased within the space of probability measures, but the choice of relaxation may differ in-between approaches (a topic we deal with in section 3.1).

Convexification For convexification, one *lifts* the manifold \mathcal{M} into $\mathbb{P}_2(\mathcal{M})$, which is the Wasserstein space of order 2 that is defined in eq. (4). More precisely, the idea is replace eq. (1) with the convex optimisation problem

$$\inf_{\mu \in \mathbb{P}_2(\mathcal{M})} \left\{ \int_{\mathcal{M}} F(p) d\mu(p) \right\}. \quad (6)$$

Projection If one can guarantee existence of solutions to eq. (6), then such a solution $\mu^* \in \mathbb{P}_2(\mathcal{M})$ can be projected back onto the manifold \mathcal{M} through a (possibly set-valued) (Riemannian) barycentre mapping

$$P: \mathbb{P}_2(\mathcal{M}) \rightrightarrows \mathcal{M} \quad \text{where} \quad P(\mu) := \operatorname{argmin}_{q \in \mathcal{M}} \left\{ \int_{\mathcal{M}} d_{\mathcal{M}}(p, q)^2 d\mu(p) \right\} \text{ for } \mu \in \mathbb{P}_2(\mathcal{M}). \quad (7)$$

The above is by [43, Proposition 1] well-defined for all measures $\mu \in \mathbb{P}_2(\mathcal{M})$ whenever \mathcal{M} is geodesically connected. For connected manifolds existence holds only locally, i.e., for measures with support on a geodesically connected subset.

Furthermore, if μ^* is a unique solution to eq. (6) that is given as a Dirac measure, i.e., $\mu^* = \delta_q$ for some $q \in \mathcal{M}$, then $q \in \mathcal{M}$ also solves eq. (1) and it is recovered by the barycenter mapping. However, μ^* may differ from a Dirac measure, e.g., it may even be diffuse.

Discretisation A numerical implementation for a method that solves eq. (6) needs to include a discretisation. A common approach is to restrict the control variable in the optimisation to an appropriate finite dimensional subspace of $\mathbb{P}_2(\mathcal{M})$. This procedure will give rise to a *discretisation error*.

For the (geodesically) connected Riemannian manifold \mathcal{M} , there is a natural discretisation of $\mathbb{P}_2(\mathcal{M})$ obtained by considering the sub-space of measures that are linear combinations of Dirac distributions located at finitely many sample points in \mathcal{M} . To formalise this, we note first that *any* measure $\mu \in \mathbb{P}_2(\mathcal{M})$ can be approximated by a sum of Dirac measures [40, Lemma 6.2]. Hence, it is natural to consider probability measures on \mathcal{M} that are given as linear combinations of Dirac measures, i.e., measures of the form

$$\sum_{p \in \mathcal{X}} \beta_p \delta_p \quad \text{for some } \beta_p \in \mathbb{R} \text{ with fixed finite set } \mathcal{X} \subset \mathcal{M} \text{ (sampling points)}. \quad (8)$$

Note that the linear combination in eq. (8) defines a probability measure on \mathcal{M} whenever the coefficient array $\beta = (\beta_p)_{p \in \mathcal{X}} \in \mathbb{R}^{|\mathcal{X}|}$ in eq. (8) is in the unit $|\mathcal{X}|$ -dimensional simplex:

$$\beta \in \Delta^{|\mathcal{X}|} := \{x \in \mathbb{R}^{|\mathcal{X}|} \mid x \geq 0, \mathbf{1} \cdot x = 1\}. \quad (9)$$

To summarise, the set of measures on \mathcal{M} of the form in eq. (8) for some fixed $\mathcal{X} \subset \mathcal{M}$ is a discretisation of $\mathbb{P}_2(\mathcal{M})$, i.e., a finite dimensional subspace of $\mathbb{P}_2(\mathcal{M})$. Note also that if $\mu \in \mathbb{P}_2(\mathcal{M})$ is a measure of the form eq. (8), then integrating $F: \mathcal{M} \rightarrow \mathbb{R}$ against μ reduces to taking the inner product of $F_{\mathcal{X}} \in \mathbb{R}^{|\mathcal{X}|}$ (the array obtained by sampling F on \mathcal{X}) and $\beta \in \Delta^{|\mathcal{X}|} \subset \mathbb{R}^{|\mathcal{X}|}$:

$$\int_{\mathcal{M}} F(p) d\mu(p) = F_{\mathcal{X}} \cdot \beta \quad \text{where } F_{\mathcal{X}} := (F(p))_{p \in \mathcal{X}} \in \mathbb{R}^{|\mathcal{X}|}. \quad (10)$$

Relaxation Discretising the lifted problem eq. (6) by eq. (10) amounts to minimising

$$\inf_{\beta \in \mathbb{R}^{|\mathcal{X}|}} \left\{ F_{\mathcal{X}} \cdot \beta + \chi_{\Delta^{|\mathcal{X}|}}(\beta) \right\}, \quad (11)$$

where $\chi_{\Delta^{|\mathcal{X}|}}: \mathbb{R}^{|\mathcal{X}|} \rightarrow \{0, \infty\}$ is defined as

$$\chi_{\Delta^{|\mathcal{X}|}}(\beta) := \begin{cases} 0, & \text{if } \beta \in \Delta^{|\mathcal{X}|}, \\ \infty, & \text{otherwise.} \end{cases} \quad (12)$$

The solution to optimisation problem eq. (11) will collapse into the specific sampling point $p \in \mathcal{X}$ where F has its lowest value. The corresponding barycentre will then equal that point, so without further adaptations to the optimisation problem, one will need a very fine mesh – and unfeasibly many sample points – to get an accurate approximation of the global minimiser to F . A typical approach to overcome this, is to make adaptations to the discretized energy eq. (11) such that β has multiple non-zero entries. The barycentre mapping then allows one to find values between the sampling points so that one is no longer directly restricted by the mesh density.

Approaches for relaxation vary depending on the underlying optimisation problem [45, 72, 73]. Typically, the optimisation problem after relaxation is computationally feasible. However, it is difficult to perform a mathematical analysis of the errors due to convexification, projection, discretisation and relaxation. This still remains an open problem in the general setting.

3 Ellipsoidal support lifting for Riemannian manifolds

We propose a new relaxation method for measure-based lifting on \mathcal{M} (section 3.1), that overcomes collapsing into a single point in the sampling set and that allows an error analysis (section 3.2). Additionally, it yields a computationally feasible algorithm (section 3.3). The main theoretical results stated in section 3.2 are proved in section 4. Throughout this section, ω_d denotes the volume of a d -dimensional unit ball.

3.1 A new relaxation strategy

Adding the Tikhonov-type regulariser $\beta \mapsto \gamma \|\beta\|_2^2 / 2 |\mathcal{X}|^\eta$ as a relaxation on the coefficients β in eq. (11) leads to the following variational problem:

$$\inf_{\beta \in \mathbb{R}^{|\mathcal{X}|}} \left\{ F_{\mathcal{X}} \cdot \beta + \chi_{\Delta^{|\mathcal{X}|}}(\beta) + \frac{\gamma}{2 |\mathcal{X}|^\eta} \|\beta\|_2^2 \right\} \quad \text{for regularisation parameters } \gamma > 0 \text{ and } \eta \in \mathbb{R}. \quad (13)$$

The projection map in eq. (7) applied to the measure $\mu^* := \sum_{p \in \mathcal{X}} \beta_p^* \delta_p$ that solves eq. (13) yields the barycentre, which is the point in \mathcal{M} given as

$$P\left(\sum_{p \in \mathcal{X}} \beta_p^* \delta_p\right) = \operatorname{argmin}_{q \in \mathcal{M}} \left\{ \sum_{p \in \mathcal{X}} \beta_p^* d_{\mathcal{M}}(p, q)^2 \right\}. \quad (14)$$

The rationale for this choice of relaxation is threefold.

Computational feasibility The first rationale for choosing a Tikhonov type regulariser relates to computational feasibility. In fact, the (finite-dimensional) minimisation in eq. (13) is not only strongly convex, its unique minimiser can be expressed in closed form. To see this, note first that the unique minimiser $\beta^* \in \Delta^{|\mathcal{X}|}$ to eq. (13) can be expressed more conveniently by rewriting the objective functional

$$\begin{aligned} \beta^* &= \operatorname{argmin}_{\beta \in \mathbb{R}^{|\mathcal{X}|}} \left\{ F_{\mathcal{X}} \cdot \beta + \chi_{\Delta^{|\mathcal{X}|}}(\beta) + \frac{\gamma}{2 |\mathcal{X}|^\eta} \|\beta\|_2^2 \right\} \\ &= \operatorname{argmin}_{\beta \in \mathbb{R}^{|\mathcal{X}|}} \left\{ \frac{\gamma}{2 |\mathcal{X}|^\eta} \left\| \beta + \frac{|\mathcal{X}|^\eta}{\gamma} F_{\mathcal{X}} \right\|_2^2 + \chi_{\Delta^{|\mathcal{X}|}}(\beta) \right\} = \Pi_{\Delta^{|\mathcal{X}|}} \left(-\frac{|\mathcal{X}|^\eta}{\gamma} F_{\mathcal{X}} \right), \end{aligned} \quad (15)$$

where $\Pi_{\Delta^{|\mathcal{X}|}}: \mathbb{R}^{|\mathcal{X}|} \rightarrow \Delta^{|\mathcal{X}|}$ is the projection onto the unit $|\mathcal{X}|$ -simplex $\Delta^{|\mathcal{X}|}$ in eq. (9). As we show next, the final term in eq. (15) has a closed-form expression that can be computed efficiently.

Lemma 3.1 ([21, Lemma 1&2]). *For any $x \in \mathbb{R}^d$ with $x_{(1)} \geq \dots \geq x_{(d)}$ are the components of x sorted in descending order, there is a unique cut-off integer $J = J(x)$, so that*

$$x_{(J)} \geq \frac{1}{J} \left(\sum_{j=1}^J x_{(j)} \right) - \frac{1}{J} \geq x_{(J+1)} \quad \text{or} \quad x_{(d)} \geq \frac{1}{J} \left(\sum_{j=1}^J x_{(j)} \right) - \frac{1}{J}. \quad (16)$$

holds.

Then, the projection $\Pi_{\Delta^d}: \mathbb{R}^d \rightarrow \Delta^d$ of \mathbb{R}^d onto the d -simplex Δ^d can be computed as

$$\Pi_{\Delta^d}(x) = \left(x - \frac{1}{J} \left(\sum_{j=1}^J x_{(j)} \right) + \frac{1}{J} \right)_+. \quad (17)$$

In particular, note that $J = \|\Pi_{\Delta^d}(x)\|_0$ holds.

Remark 3.2. In the analysis of the relaxation method – in particular in the proof of theorem 3.6 – it will be important to consider the uniqueness of the cut-off integer J closer. That is, observe that $n \mapsto \frac{1}{n} \left(\sum_{j=1}^n x_{(j)} \right) - \frac{1}{n}$ is monotonically increasing. Then, the uniqueness of the cut-off integer from lemma 3.1 tells us that $\|(x - \frac{1}{J'} \left(\sum_{j=1}^{J'} x_{(j)} \right) + \frac{1}{J'})_+\|_0 < J$ is equivalent to having $J' > J$, i.e., there will be too few non-zero coefficients iff J' “were to be used as cut-off integer”. Conversely, choosing an $J'' < J$ is equivalent to having too many non-zero coefficients.

Sparsity and locality of the measure The second rationale relates to having a local and sparse measure concentrated around the global minimiser of eq. (1) (theorem 3.6) for properly chosen regularisation parameters γ and η , which is key for a well-posed Riemannian barycentre and for establishing error bounds (theorem 3.7). Note that the coefficients generated by the Tikhonov-type lifting scheme in eq. (13) mimic the shape of the Riemannian Hessian of the objective at the global minimiser p^* . This can be seen through Taylor expansion

$$\begin{aligned} \beta_p^* &= \Pi_{\Delta^{|\mathcal{X}|}} \left(-\frac{|\mathcal{X}|^\eta}{\gamma} F_{\mathcal{X}} \right)_p = \left(-\frac{|\mathcal{X}|^\eta}{\gamma} F(p) - \frac{1}{J} \left(\sum_{j=1}^J -\frac{|\mathcal{X}|^\eta}{\gamma} F(p_{(j)}) - 1 \right) \right)_+ \\ &= \left(\frac{1}{J} + \frac{|\mathcal{X}|^\eta}{\gamma} \left(\frac{1}{J} \left(\sum_{j=1}^J F(p_{(j)}) \right) - F(p) \right) \right)_+ \\ &\approx \left(C_{\mathcal{X}}^{\eta, \gamma} - \frac{|\mathcal{X}|^\eta}{2\gamma J} \text{Hess}_{p^*} F(\log_{p^*}(p), \log_{p^*}(p)) \right)_+ \end{aligned} \quad (18)$$

for $p \in \mathcal{X}$ and where

$$C_{\mathcal{X}}^{\eta, \gamma} := \frac{1}{J} + \frac{|\mathcal{X}|^\eta}{2\gamma} \frac{1}{J} \left(\sum_{j=1}^J \text{Hess}_{p^*} F(\log_{p^*}(p_{(j)}), \log_{p^*}(p_{(j)})) \right).$$

From eq. (18) we also see that the coefficients of β become zero outside some level set of the $p \mapsto \text{Hess}_{p^*} F(\log_{p^*}(p), \log_{p^*}(p))$ mapping.

For the approximation to become exact – while ensuring a sparse and local measure as suggested above – we will show in the following that we need to set

$$\gamma := \frac{1}{2(d+2)} J_0^{\frac{d+2}{d}} \sqrt{\det(\text{Hess}_{p^*} F) \left(\frac{\text{vol}(\mathcal{M})}{\omega_d} \right)^2}. \quad (19)$$

where $d := \dim(\mathcal{M})$ and J_0 is roughly the amount of non-zero coefficients one chooses to have, and the parameter $\eta \in (1/(d+1), 2/d)$.

Resolving collapsing The third rationale relates to avoiding collapsing into a single point. Consider the optimisation problem eq. (13) for setting the coefficients β . As sparse (and local) solutions have been suggested above to be key for the lifting approach, one might wonder why a Tikhonov-type ℓ^2 -regulariser has been chosen rather than ℓ^1 . The reason is that every ℓ^1 -regulariser will collapse into a single point in practice. Indeed

$$\inf_{\beta \in \mathbb{R}^{|\mathcal{X}|}} \left\{ F_{\mathcal{X}} \cdot \beta + \chi_{\Delta^{|\mathcal{X}|}}(\beta) + \|\beta\|_1 \right\} = \inf_{\beta \in \Delta^{|\mathcal{X}|}} \left\{ F_{\mathcal{X}} \cdot \beta + \mathbf{1} \cdot \beta \right\} = \inf_{\beta \in \Delta^{|\mathcal{X}|}} \left\{ (F_{\mathcal{X}} + \mathbf{1}) \cdot \beta \right\}, \quad (20)$$

which will collapse into the specific sampling point $p \in \mathcal{X}$ where F has its lowest value. Hence, the choice for ℓ^1 is not suitable, whereas we will argue that a properly scaled Tikhonov-type regulariser can overcome the collapsing issue while preserving sparsity (theorem 3.6).

Remark 3.3. Finally, one can wonder whether any properly scaled strongly convex regulariser could yield similar or better results to using a Tikhonov-type regulariser as a relaxation on the coefficients β – that is, on top of computing the coefficients in a computationally feasible manner and overcoming the collapsing issue while preserving sparsity and locality.

At this point remark 3.3 is an open question as the lack of closed form solutions for the resulting optimisation problem makes analysis difficult. Indeed, even for simple ℓ^s -regularisation for $s \neq 1, 2$ these solutions are not available to the best of our knowledge. Nevertheless, there is a case to make that these methods will not outperform our approach. That is, the error rate on the proposed scheme (theorem 3.7) already gives a curse-of-dimensionality-rate which is the best we can hope for due to the non-convexity. Besides that, and even with the analysis overcome, computational infeasibility due to the lack of closed form solutions will pose a serious issue for practical use. In summary, the Tikhonov-type relaxation arguably gives us all we can expect for this class of lifting-based schemes.

3.2 Main theoretical results

As suggested above with *locality and sparsity*, we will only be interested in the *local* behaviour of functions around its minimiser. In particular, we will be interested in certain ellipsoids generated by the Riemannian Hessian of the function F at its minimiser. More generally, one can define ellipsoids generated by symmetric positive definite bi-linear forms.

Definition 3.4. Let \mathcal{M} be a Riemannian manifold with dimension $d := \dim(\mathcal{M})$, $p \in \mathcal{M}$, and let $Q: \mathcal{T}_p\mathcal{M} \times \mathcal{T}_p\mathcal{M} \rightarrow \mathbb{R}$ be a symmetric positive definite bi-linear form. We define the open ellipsoid $\mathcal{E}_r^Q(p) \subset \mathcal{M}$ with radius $r > 0$ around $p \in \mathcal{M}$ generated by Q as

$$\mathcal{E}_r^Q(p) := \{q \in \mathcal{M} \mid Q(\log_p q, \log_p q) < \sqrt[d]{\det(Q)} r^2\}. \quad (21)$$

For the following results to hold it is key that the sampling set \mathcal{X} is “*distributed uniformly*” over the manifold. What it means for sampling sets \mathcal{X} to cover the manifold well will be formalized by the *sampling set’s ability to approximate local integration*. For completeness, the definition used throughout this work is provided below, but for the reader’s convenience it will be unpacked in section 4.1 as it is rather technical.

Definition 3.5 (η -local low-discrepancy sequence). Let \mathcal{M} be a finite-volume Riemannian manifold with dimension $d := \dim(\mathcal{M})$ and $S(\mathcal{M}) := \{\mathcal{X} \subset \mathcal{M} \mid |\mathcal{X}| < \infty\}$ denotes the collection of all finite sampling sets in \mathcal{M} . A sequence $(\mathcal{X}_m)_{m=1}^\infty \subset S(\mathcal{M})$ is an η -local low-discrepancy sequence on \mathcal{M} for some $\eta \in \mathbb{R}$ such that $1/(d+1) < \eta < 2/d$ if $|\mathcal{X}_m| < |\mathcal{X}_{m+1}|$ for all $m \in \mathbb{N}$ and for any symmetric positive-definite bi-linear form $Q: \mathcal{T}_p\mathcal{M} \times \mathcal{T}_p\mathcal{M} \rightarrow \mathbb{R}$ at any point $p \in \mathcal{M}$ and for

$$r_m := \sqrt[d]{C \frac{\text{vol}(\mathcal{M})}{\omega_d}} |\mathcal{X}_m|^{-\frac{1+\eta}{d+2}} \quad \text{where } C \geq 1 \text{ is any constant}$$

the local integration approximation has the following asymptotic behaviour as $|\mathcal{X}_m| \rightarrow \infty$:

1. Local integration approximation for constant functions:

$$\left| \frac{|\mathcal{E}_{r_m}^Q(p) \cap \mathcal{X}_m|}{|\mathcal{X}_m|} - \frac{\text{vol}(\mathcal{E}_{r_m}^Q(p))}{\text{vol}(\mathcal{M})} \right| \in \mathcal{O}\left(|\mathcal{X}_m|^{-\frac{(d+1)(1+\eta)}{d+2}}\right) \quad (22)$$

2. Local integration approximation for bi-linear forms:

$$\left| \sum_{q \in \mathcal{E}_{r_m}^Q(p) \cap \mathcal{X}_m} \frac{Q(\log_p(q), \log_p(q))}{|\mathcal{X}_m|} - \frac{\int_{\mathcal{E}_{r_m}^Q(p)} Q(\log_p(q), \log_p(q)) \, dq}{\text{vol}(\mathcal{M})} \right| \in \mathcal{O}\left(|\mathcal{X}_m|^{-\frac{(d+3)(1+\eta)}{d+2}}\right). \quad (23)$$

With the above notion of η -local low-discrepancy sequence of sampling sets on \mathcal{M} , we can formulate the main results, theorems 3.6 and 3.7. The proofs are provided in section 4.

Theorem 3.6 justifies the choice of Tikhonov-type regularisation term in eq. (13) and can be summarized by two important insights that hold when the corresponding regularisation parameter γ is appropriately chosen. The first insight is that non-zero coefficients associated with the probability measure will be concentrated on an ellipsoid around the global minimiser, the second is that there will be very few non-zero coefficients, i.e., β^* is sparse:

Theorem 3.6 (Sparsity & locality of the optimal measure). *Consider the minimisation in eq. (13) where $F: \mathcal{M} \rightarrow \mathbb{R}$ is a smooth function defined on a finite-volume Riemannian manifold \mathcal{M} with dimension $d := \dim(\mathcal{M})$. Assume also that F has a unique global minimiser $p^* \in \mathcal{M}$ and its Riemannian Hessian $\text{Hess}_{p^*} F$ is positive definite at p^* . Furthermore, assume $(\mathcal{X}_m)_{m=1}^\infty$ is an η -local low-discrepancy sequence with $1/(d+1) < \eta < 2/d$. Finally, set γ as in eq. (19) for some $J_0 \geq 3^{-\frac{d}{d+2}}$.*

Then, there exists $m' \in \mathbb{N}$ such that for all $m \geq m'$ the points $p \in \mathcal{X}_m$ with non-zero coefficients must lie in an ellipsoid $\mathcal{E}_{R_m}^Q(p^)$ of the type in eq. (21) where $Q: \mathcal{T}_p \mathcal{M} \times \mathcal{T}_p \mathcal{M} \rightarrow \mathbb{R}$ is $Q := \text{Hess}_{p^*} F$ and $R_m > 0$ given as*

$$R_m := \sqrt[d]{J_0 \frac{\text{vol}(\mathcal{M})}{\omega_d}} |\mathcal{X}_m|^{-\frac{1+\eta}{d+2}}. \quad (24)$$

Furthermore, if $\beta_m^ \in \Delta^{|\mathcal{X}_m|}$ is the unique minimiser to eq. (13) for sampling set \mathcal{X}_m , then*

$$3^{-\frac{d}{d+2}} J_0 |\mathcal{X}_m|^{\frac{2-d\eta}{d+2}} \leq \|\beta_m^*\|_0 \leq J_0 |\mathcal{X}_m|^{\frac{2-d\eta}{d+2}}. \quad (25)$$

The next result, theorem 3.7, establishes existence and uniqueness of the barycentre and provides a bound on the error made by convexification, projection, discretisation, and relaxation:

Theorem 3.7 (Well-posedness & error bounds). *Consider the minimisation in eq. (13) with the same assumptions as in theorem 3.6.*

Then, there exists $m' \in \mathbb{N}$ such that for all $m \geq m'$ the Riemannian barycentre w.r.t. the probability measure given by the unique minimiser $\beta_m^ \in \Delta^{|\mathcal{X}_m|}$ to eq. (13) for sampling set \mathcal{X}_m exists and is single valued, i.e.,*

$$p_{\mathcal{X}_m}^* := \underset{q \in \mathcal{M}}{\text{argmin}} \left\{ \sum_{p \in \mathcal{X}_m} (\beta_m^*)_p d_{\mathcal{M}}(p, q)^2 \right\} \quad \text{is well-defined point in } \mathcal{M}. \quad (26)$$

Furthermore, the distance between this unique barycentre $p_{\mathcal{X}_m}^$ and the unique minimiser p^* of F is bounded as*

$$d_{\mathcal{M}}(p_{\mathcal{X}_m}^*, p^*) \leq 2 \sqrt{\frac{\sqrt[d]{\det(\text{Hess}_{p^*} F)}}{\lambda_{\min}(\text{Hess}_{p^*} F)}} R_m \quad \text{with } R_m > 0 \text{ given as in eq. (24)}. \quad (27)$$

In the above, $\lambda_{\min}(\text{Hess}_{p^} F)$ is the smallest eigenvalue of the symmetric positive-definite bilinear form $\text{Hess}_{p^*} F: \mathcal{T}_{p^*} \mathcal{M} \times \mathcal{T}_{p^*} \mathcal{M} \rightarrow \mathbb{R}$.*

3.3 Algorithm

From Karcher [38, Theorem 1.2] we know that the problem eq. (26) restricted to a small enough geodesic ball around the global minimiser p^* – rather than the full manifold \mathcal{M} – is actually convex. In other words, the theoretical results suggest that for $1/(\dim(\mathcal{M}) + 1) < \eta < 2/\dim(\mathcal{M})$ and a proper choice of regularisation parameter $\gamma > 0$ and sampling set $\mathcal{X} \subset \mathcal{M}$ one can use a Riemannian gradient descent scheme – initialised with the point $p \in \mathcal{X}$ with the highest value for β_p^* – to solve the optimisation in eq. (14) and thereby compute the Riemannian barycentre for approximating the solution to the non-convex minimisation problem in eq. (1). If the gradient step size is $1/2$, then this scheme reads as

$$p^{k+1} := \exp_{p^k} \left(\sum_{p \in \mathcal{X}} \beta_p^* \log_{p^k}(p) \right). \quad (28)$$

To see this, simply note that the gradient of $d_{\mathcal{M}}(p, \cdot)^2$ at some point $q \in \mathcal{M}$ is given as

$$\text{grad}(d_{\mathcal{M}}(p, \cdot)^2)|_q = -2 \log_q(p) \quad \text{for } q \in \mathcal{M}.$$

Combined with the computation of the coefficients, the full optimisation scheme is outlined in algorithm 1. We will refer to this approach as *ellipsoidal support lifting* (ESL).

Algorithm 1 The ellipsoidal support lifting (ESL) scheme

Initialisation: $\mathcal{X} \subset \mathcal{M}$, $d := \dim(\mathcal{M})$, $\gamma > 0$, $\eta \in (\frac{1}{d+1}, \frac{2}{d})$, $k := 0$

$$\beta^* = \Pi_{\Delta|\mathcal{X}|} \left(-\frac{|\mathcal{X}|^\eta}{\gamma} F_{\mathcal{X}} \right)$$

$$p^0 := \operatorname{argmax}_{p \in \mathcal{X}} \beta_p^*$$

while not converged **do**

$$p^{k+1} := \exp_{p^k} \left(\sum_{p \in \mathcal{X}} \beta_p^* \log_{p^k}(p) \right)$$

$$k := k + 1$$

end while

Note that it remains to have a practically realisable scheme for choosing/constructing \mathcal{X} and γ . Without going too much into detail, the sampling set \mathcal{X} – or rather the sequence of sampling sets $(\mathcal{X}_m)_{m=1}^\infty$ – can be constructed through mesh refinement, i.e., one starts from some small uniformly distributed set of points \mathcal{X}_0 , constructs a triangulation, and applies some refinement rule. Choosing such a \mathcal{X}_0 and refinement rule is highly dependent on the manifold of interest and the application. Both will be addressed below in the Cryo-EM case study in section 6. Then, the most challenging aspect in constructing γ will be determining the (determinant of the) Riemannian Hessian. In exceptional cases the Hessian is known, but in general one will need to resort to approximations. One final consequence of our theoretical analysis is the following result, which provides such an approximation for the γ in eq. (19) required by the main results.

Proposition 3.8. *Let $F: \mathcal{M} \rightarrow \mathbb{R}$ be a smooth function defined on a finite-volume Riemannian manifold \mathcal{M} with dimension $d := \dim(\mathcal{M})$. Assume also that F has a unique global minimiser $p^* \in \mathcal{M}$ and its Riemannian Hessian $\text{Hess}_{p^*} F$ is positive definite at p^* . Finally, define γ as in eq. (19) for some $J_0 \geq 1$.*

Then, for any η -local low-discrepancy sequence $(\mathcal{X}_m)_{m=1}^\infty$ with $1/(d+1) < \eta < 2/d$, each

\mathcal{X}_m with labeled points $p_{(1)}^m, \dots, p_{(|\mathcal{X}_m|)}^m$ sorted such that $F(p_{(1)}^m) \leq \dots \leq F(p_{(|\mathcal{X}_m|)}^m)$, we have

$$\lim_{m \rightarrow \infty} \frac{1}{2} J_0^{\frac{d+2}{d}} \left(\frac{|\mathcal{X}_m|}{J_m} \right)^{\frac{2}{d}} \left(F(p_{(J_m+1)}^m) - \frac{1}{J_m} \sum_{j=1}^{J_m} F(p_{(j)}^m) \right) = \gamma, \quad (29)$$

where $J_m := \lfloor J_0 |\mathcal{X}_m|^{\frac{2-d\eta}{d+2}} \rfloor$.

4 Proofs of the main results

This part focuses on the proofs of theorems 3.6 and 3.7 and proposition 3.8. The starting point is to elaborate on the notion of an η -local low-discrepancy sequence (section 4.1), which is followed by the proof of theorem 3.6 (section 4.2), i.e., showing that eq. (15) generates a sparse measure concentrated on an ellipsoid. The latter also yields techniques for proving theorem 3.7 (section 4.3), which gives well-posedness of the barycentre and error bounds on algorithm 1, and for proving proposition 3.8 (section 4.4).

4.1 A note on η -local low-discrepancy sequences

As definition 3.5 is rather technical, we will briefly unpack it. There are four main choices to justify: the choice of the sets we want to integrate over, the choice of functions we integrate, the choice of the decay rates on the discrepancies we ask for, and the choice of the bounds for the parameter η in definition 3.5. Existence of such sequences will be discussed afterwards.

Choice of sets First consider the sets $\mathcal{E}_{r_m}^Q(p)$. As indicated before, the solution to eq. (13) yields a sparse measure that is supported around the global minimiser of the function F . The shape of the region containing the support is determined by the Riemannian Hessian, if it is a symmetric positive-definite bi-linear form, and its size scales with radius

$$r_m = \sqrt[d]{\frac{\text{vol}(\mathcal{M})}{\omega_d}} |\mathcal{X}_m|^{-\frac{1+\eta}{d+2}},$$

or with this radius multiplied with any constant larger than 1. In other words, we are only concerned with local integration.

Choice of functions This naturally motivates the choice of functions. Since the sampling sets only have to integrate accurately in a local neighbourhood, they only need to be accurate enough on local approximations of functions. In particular, the integration scheme only needs to be able to integrate a Taylor expansion of a function around its minimiser up to second-order term. In other words, we only need to be able to integrate over constants eq. (22) and Riemannian Hessians eq. (23), which come in the form of a symmetric positive-definite bi-linear forms, as the gradient is zero at the global minimiser.

Choice of decay rates and η bounds The rates in eqs. (22) and (23) and the η bounds are chosen to ensure that, as the sample set size $|\mathcal{X}_m|$ increases, the number of points in the ellipsoids $\mathcal{E}_{r_m}^Q(p)$ approaches infinity. This is despite the fact that the size of the ellipsoids vanishes asymptotically. More precisely, in lemma 4.2 it will be shown that

$$\text{vol}(\mathcal{E}_{r_m}^Q(p)) = \omega_d r_m^d + \mathcal{O}(r_m^{d+1}) = \omega_d r_m^d + \mathcal{O}(|\mathcal{X}_m|^{-\frac{(d+1)(1+\eta)}{d+2}}), \quad (30)$$

and

$$\begin{aligned} \int_{\mathcal{E}_{r_m}^Q(p)} Q(\log_p(q), \log_p(q)) dq &= \sqrt[d]{\det(Q)} \frac{\omega_d d}{d+2} r_m^{d+2} + \mathcal{O}(r_m^{d+3}) \\ &= \sqrt[d]{\det(Q)} \frac{\omega_d d}{d+2} r_m^{d+2} + \mathcal{O}(|\mathcal{X}_m|^{-\frac{(d+3)(1+\eta)}{d+2}}). \end{aligned} \quad (31)$$

Note that for $1/(d+1) < \eta < 2/d$ the number of points that would fit in an ellipsoid of radius $r_m = \sqrt[d]{\frac{\text{vol}(\mathcal{M})}{\omega_d}} |\mathcal{X}_m|^{-\frac{1+\eta}{d+2}}$ grows indefinitely. Indeed,

$$\frac{\text{vol}(\mathcal{E}_{r_m}^Q(p))}{\text{vol}(\mathcal{M})} |\mathcal{X}_m| = |\mathcal{X}_m|^{\frac{2-d\eta}{d+2}} + \mathcal{O}(|\mathcal{X}_m|^{\frac{1-(d+1)\eta}{d+2}}), \quad (32)$$

and the first term on the right hand side will grow infinitely large, whereas the second term vanishes as $m \rightarrow \infty$, i.e., the number of points in this family of ellipsoids grows arbitrarily large even though the sets themselves contract.

Remark 4.1. *Thus, we simply ask in definition 3.5 that for an increasing amount of points in a contracting local volume, the approximations in eqs. (22) and (23) should be as exact as the leading term in eq. (30) respectively eq. (31).*

Although definition 3.5 – accompanied with this motivation – sounds reasonable, existence of such sequences is still open, as analysis of error rates of sampling sets is typically developed for global integration [17]. To take a first step, the numerical experiments provided in section 7 – that show the error rates discussed next – will give some additional empirical evidence for the η -local low-discrepancy property being well-defined.

4.2 Sparse and concentrated measures through relaxation

In order to prove theorem 3.6, we will argue that the points with non-zero coefficients must be contained in an ellipsoid and that the scaling behaviour of the ellipsoid's volume yields a bound for the scaling of number of non-zero coefficients. The following lemma allows us to approximate ellipsoid volumes and provides a second integration approximation, which will be key for the proof of the main result.

Lemma 4.2. *Let \mathcal{M} be a Riemannian manifold with dimension $d := \dim(\mathcal{M})$, $p \in \mathcal{M}$, and let $Q: \mathcal{T}_p \mathcal{M} \times \mathcal{T}_p \mathcal{M} \rightarrow \mathbb{R}$ be a symmetric positive definite bi-linear form. Then, for radii $r \rightarrow 0$ we have*

$$\text{vol}(\mathcal{E}_r^Q(p)) = \omega_d r^d + \mathcal{O}(r^{d+1}) \quad (33)$$

and

$$\int_{\mathcal{E}_r^Q(p)} Q(\log_p(q), \log_p(q)) dq = \sqrt[d]{\det(Q)} \frac{\omega_d d}{d+2} r^{d+2} + \mathcal{O}(r^{d+3}). \quad (34)$$

Proof. Let $\{X_i\}_{i=1}^d \subset \mathcal{T}_p \mathcal{M}$ be an orthonormal basis of eigenvectors of Q with corresponding eigenvalues $\lambda_i(Q)$. Furthermore, let $\phi_{\mathcal{E}}: \mathcal{E}_r^Q(p) \rightarrow \mathbb{R}^d$ be the *re-scaled* normal coordinate chart generated by $\{X_i\}_{i=1}^d$, with the i :th component given by

$$\phi_{\mathcal{E}}(q)_i := \frac{\sqrt{\lambda_i(Q)}}{\sqrt[d]{\det(Q)}} (X_i, \log_p(q))_p. \quad (35)$$

The inverse $\phi_{\mathcal{E}}^{-1}: \phi_{\mathcal{E}}(\mathcal{E}_r^Q(p)) \rightarrow \mathcal{E}_r(p)$ is then

$$\phi_{\mathcal{E}}^{-1}(x) = \exp_p \left(\sum_{i=1}^d \frac{\sqrt[d]{\det(Q)}}{\sqrt{\lambda_i(Q)}} x^i X_i \right). \quad (36)$$

Note in particular that $\phi_{\mathcal{E}}(\mathcal{E}_r^Q(p)) = \mathbb{B}_r := \{x \in \mathbb{R}^d \mid \|x\|_2 < r\}$.

Next, we claim that $\det(D_0\phi_{\mathcal{E}}^{-1}) = 1$. To see this, note first that

$$D_0\phi_{\mathcal{E}}^{-1} \left[\frac{\partial}{\partial x^i} \right] f = \frac{d}{dt} f \left(\exp_p \left(\frac{\sqrt[d]{\det(Q)}}{\sqrt{\lambda_i(Q)}} t X_i \right) \right) \Big|_{t=0} = \frac{\sqrt[d]{\det(Q)}}{\sqrt{\lambda_i(Q)}} X_i f \quad \text{for } f \in C^\infty(\mathcal{M}). \quad (37)$$

Hence, $D_0\phi_{\mathcal{E}}^{-1} \left[\frac{\partial}{\partial x^i} \right] = \frac{\sqrt[d]{\det(Q)}}{\sqrt{\lambda_i(Q)}} X_i$ and we have a diagonal matrix in the $\{X_i\}_{i=1}^d \subset \mathcal{T}_p\mathcal{M}$ basis.

This gives

$$\det(D_0\phi_{\mathcal{E}}^{-1}) = \prod_{i=1}^d \frac{\sqrt[d]{\det(Q)}}{\sqrt{\lambda_i(Q)}} = \frac{\sqrt[d]{\det(Q)}}{\prod_{i=1}^d \sqrt{\lambda_i(Q)}} = 1 \quad \text{as } \det(Q) = \prod_{i=1}^d \lambda_i(Q), \quad (38)$$

which proves that $\det(D_0\phi_{\mathcal{E}}^{-1}) = 1$.

Using this result, the proof of the claim in eq. (33) follows directly from the following calculation:

$$\begin{aligned} \text{vol}(\mathcal{E}_r^Q(p)) &= \int_{\mathcal{E}_r^Q(p)} dq = \int_{\mathbb{B}_r} |\det(D_x\phi_{\mathcal{E}}^{-1})| dx = \int_{\mathbb{B}_r} \det(D_x\phi_{\mathcal{E}}^{-1}) dx \\ &= \int_{\mathbb{B}_r} \det(D_0\phi_{\mathcal{E}}^{-1}) + \mathcal{O}(r) dx = \text{vol}(\mathbb{B}_r) + \mathcal{O}(r^{d+1}) = \omega_d r^d + \mathcal{O}(r^{d+1}), \end{aligned}$$

where we used in the third equality the fact that for small enough radius r the determinant must have a constant (positive) sign. The fourth equality stems from a Taylor expansion around 0 – this is justified, as the differential of the local chart varies smoothly and so will its eigenvalues, and hence also its determinant.

Similarly, the proof of equality eq. (34) reads as follows:

$$\begin{aligned} \int_{\mathcal{E}_r^Q(p)} Q(\log_p(q), \log_p(q)) dq &= \int_{\mathbb{B}_r} Q(\log_p(\phi_{\mathcal{E}}^{-1}(x)), \log_p(\phi_{\mathcal{E}}^{-1}(x))) \det(D_x\phi_{\mathcal{E}}^{-1}) dx \\ &= \sqrt[d]{\det(Q)} \int_{\mathbb{B}_r} \|x\|_2^2 \det(D_x\phi_{\mathcal{E}}^{-1}) dx = \sqrt[d]{\det(Q)} \int_{\mathbb{B}_r} [\|x\|_2^2 \det(D_0\phi_{\mathcal{E}}^{-1}) + \mathcal{O}(r^3)] dx \\ &= \sqrt[d]{\det(Q)} \int_{\mathbb{B}_r} \|x\|_2^2 dx + \mathcal{O}(r^{d+3}) = \sqrt[d]{\det(Q)} \frac{\omega_d d}{d+2} r^{d+2} + \mathcal{O}(r^{d+3}). \end{aligned}$$

The 2:nd equality above follows from $Q(\log_p(\phi_{\mathcal{E}}^{-1}(x)), \log_p(\phi_{\mathcal{E}}^{-1}(x))) = \sqrt[d]{\det(Q)} \|x\|_2^2$. \square

The following lemma is a consequence of Lemma 4.2 and essential for the proof of theorem 3.6.

Lemma 4.3. *Let \mathcal{M} be a finite-volume Riemannian manifold with dimension $d := \dim(\mathcal{M})$. Consider any point $p \in \mathcal{M}$, symmetric positive definite bi-linear form $Q: \mathcal{T}_p\mathcal{M} \times \mathcal{T}_p\mathcal{M} \rightarrow \mathbb{R}$, constant $C \geq 1$ and $0 < \epsilon < \frac{1}{2}$. Furthermore, assume that $(\mathcal{X}_m)_{m=1}^\infty$ is an η -local low-discrepancy sequence with $1/(d+1) < \eta < 2/d$.*

1. Define $(J'_m)_{m=1}^\infty \subset \mathbb{N}$ by $J'_m := \lceil C|\mathcal{X}_m|^{\frac{2-d\eta}{d+2}} \rceil$, and define the sequences of vanishing radii $(R'_m)_{m=1}^\infty \subset \mathbb{R}_+$ and $(r'_m)_{m=1}^\infty \subset \mathbb{R}_+$ by $R'_m := \sqrt[d]{\frac{\text{vol}(\mathcal{M})}{\omega_d} \frac{J'_m}{|\mathcal{X}_m|}}$ and $r'_m := \sqrt{\frac{d+1+\epsilon}{d+2}} R'_m$. Then there exists $m' \in \mathbb{N}$ such that for all $m \geq m'$ we have

$$J'_m = |\mathcal{E}_{R'_m}^Q(p) \cap \mathcal{X}_m| \quad \text{and} \quad J'_m > |\mathcal{E}_{r'_m}^Q(p) \cap \mathcal{X}_m|. \quad (39)$$

2. Define $(J''_m)_{m=1}^\infty \subset \mathbb{N}$ by $J''_m := \lfloor C|\mathcal{X}_m|^{\frac{2-d\eta}{d+2}} \rfloor$, and define the sequences of vanishing radii $(R''_m)_{m=1}^\infty \subset \mathbb{R}_+$ and $(r''_m)_{m=1}^\infty \subset \mathbb{R}_+$ by $R''_m := \sqrt[d]{\frac{\text{vol}(\mathcal{M})}{\omega_d} \frac{J''_m}{|\mathcal{X}_m|}}$ and $r''_m := \sqrt{\frac{d+3-\epsilon}{d+2}} R''_m$. Then there exists $m' \in \mathbb{N}$ such that for all $m \geq m'$ we have

$$J''_m = |\mathcal{E}_{R''_m}^Q(p) \cap \mathcal{X}_m| \quad \text{and} \quad J''_m < |\mathcal{E}_{r''_m}^Q(p) \cap \mathcal{X}_m|. \quad (40)$$

Proof. Fix an η -local low-discrepancy sequence $(\mathcal{X}_m)_{m=1}^\infty \subset S(\mathcal{M})$.

To see eq. (39), first we show that

$$J'_m = |\mathcal{E}_{R'_m}^Q(p) \cap \mathcal{X}_m| \quad \text{holds for large } m. \quad (41)$$

Indeed, by eq. (33) in lemma 4.2

$$\begin{aligned} \frac{\text{vol}(\mathcal{E}_{R'_m}^F(p^*))}{\text{vol}(\mathcal{M})} |\mathcal{X}_m| &= \frac{\omega_d (R'_m)^d + \mathcal{O}((R'_m)^{d+1})}{\text{vol}(\mathcal{M})} |\mathcal{X}_m| \\ &= J'_m + \mathcal{O}(J'_m R'_m) = J'_m + \mathcal{O}(|\mathcal{X}_m|^{\frac{1-(d+1)\eta}{d+2}}) \end{aligned} \quad (42)$$

and the right-hand side approaches J'_m arbitrarily close as the remainder term vanishes because $\eta > \frac{1}{d+1}$. This tells us that the ellipsoid can hold as many points as J'_m . Combining that for large m and the η -local low-discrepancy property eq. (22) of $(\mathcal{X}_m)_{m=1}^\infty$ yields eq. (41), i.e., for large m it does hold J'_m points.

Next, the strict inequality

$$|\mathcal{E}_{r'_m}^F(p^*) \cap \mathcal{X}_m| < |\mathcal{E}_{R'_m}^F(p^*) \cap \mathcal{X}_m| \quad \text{holds for large } m, \quad (43)$$

by combining the η -local low-discrepancy property of $(\mathcal{X}_m)_{m=1}^\infty$, the fact that the amount of points in both ellipsoids grows infinitely large - even though the ellipsoid contracts as $m \rightarrow \infty$ - because $\eta < \frac{2}{d}$, and by the fixed ratio of the ellipsoid volumes

$$\lim_{m \rightarrow \infty} \frac{\text{vol}(\mathcal{E}_{r'_m}^F(p^*))}{\text{vol}(\mathcal{E}_{R'_m}^F(p^*))} = \left(\frac{d+1+\epsilon}{d+2} \right)^{\frac{d}{2}} < 1. \quad (44)$$

Combining eqs. (41) and (43) gives eq. (39).

The proof of eq. (40) is analogous to the proof of eq. (39) and is omitted. That is, the proof for the equality is exactly the same as above and for the inequality it can be shown that

$$\lim_{m \rightarrow \infty} \frac{\text{vol}(\mathcal{E}_{r''_m}^F(p^*))}{\text{vol}(\mathcal{E}_{R''_m}^F(p^*))} = \left(\frac{d+3-\epsilon}{d+2} \right)^{\frac{d}{2}} > 1, \quad (45)$$

which gives the claim as done above. \square

We are now ready to prove theorem 3.6.

Proof of theorem 3.6. Fix an η -local low-discrepancy sequence $(\mathcal{X}_m)_{m=1}^\infty \subset S(\mathcal{M})$. Define $(\beta_m^*)_{m=1}^\infty \subset \ell_0$ as the zero-padded solution operator of eq. (13), i.e.,

$$\beta_m^* := \left(\Pi_{\Delta^{|\mathcal{X}_m|}} \left(-\frac{|\mathcal{X}_m|^\eta}{\gamma} F_{\mathcal{X}_m} \right), 0, \dots \right). \quad (46)$$

Additionally, for any $m \in \mathbb{N}$ define the points $p_{(1)}^m, \dots, p_{(|\mathcal{X}_m|)}^m$ by labeling the elements of \mathcal{X}_m such that $F(p_{(1)}^m) \leq \dots \leq F(p_{(|\mathcal{X}_m|)}^m)$.

Note that with these definitions, the non-zero coefficients in β_m^* will be at the indices corresponding to the J_m smallest components of $F_{\mathcal{X}_m}$.

(i) For the first step we will (i-a) prove the upper bound in eq. (25) and (i-b) prove that the points corresponding to the non-zero coefficients lie in the ellipsoid $\mathcal{E}_{R_m}^Q(p^*)$ with $Q := \text{Hess}_{p^*} F$ with R_m as in eq. (24).

(i-a) For the upper bound in eq. (25) we will show that, for large enough m , the number of non-zero coefficients $\|\beta_m^*\|_0$ is strictly bounded by $\|\beta_m^*\|_0 < J'_m$, where

$$J'_m := \lceil J_0 |\mathcal{X}_m|^{\frac{2-d\eta}{d+2}} \rceil. \quad (47)$$

In particular, we will assume that $\|\beta_m^*\|_0 \geq J'_m$. If we can show that, for large m ,

$$\left\| \left(-\frac{|\mathcal{X}_m|^\eta}{\gamma} F_{\mathcal{X}_m} - \frac{1}{J'_m} \left(\sum_{j=1}^{J'_m} -\frac{|\mathcal{X}_m|^\eta}{\gamma} F(p_{(j)}^m) \right) + \frac{1}{J'_m} \right)_+ \right\|_0 < J'_m \quad (48)$$

holds, then also

$$\left\| \left(-\frac{|\mathcal{X}_m|^\eta}{\gamma} F_{\mathcal{X}_m} - \frac{1}{J'_m} \left(\sum_{j=1}^{J'_m} -\frac{|\mathcal{X}_m|^\eta}{\gamma} F(p_{(j)}^m) \right) + \frac{1}{J'_m} \right)_+ \right\|_0 < \|\beta_m^*\|_0 \quad (49)$$

holds by assumption. However, the latter is equivalent to $\|\beta_m^*\|_0 < J'_m$ by remark 3.2, which yields our contradiction.

It remains to show inequality eq. (48). For any point $p \in \mathcal{X}_m$,

$$\left(-\frac{|\mathcal{X}_m|^\eta}{\gamma} F(p) - \frac{1}{J'_m} \left(\sum_{j=1}^{J'_m} -\frac{|\mathcal{X}_m|^\eta}{\gamma} F(p_{(j)}^m) \right) + \frac{1}{J'_m} \right)_+ = 0 \quad (50)$$

is equivalent to

$$\left(-\frac{|\mathcal{X}_m|^\eta}{\gamma} F(p) \right) - \frac{1}{J'_m} \left(\sum_{j=1}^{J'_m} -\frac{|\mathcal{X}_m|^\eta}{\gamma} F(p_{(j)}^m) \right) + \frac{1}{J'_m} \leq 0, \quad (51)$$

or equally

$$F(p) - \frac{1}{J'_m} \sum_{j=1}^{J'_m} F(p_{(j)}^m) \geq \frac{\gamma}{J'_m |\mathcal{X}_m|^\eta}. \quad (52)$$

We will show that, for large enough m , too many points p – that is more than $|\mathcal{X}_m| - J'_m$ – satisfy the last inequality eq. (52); hence there are less than J'_m points $p \in \mathcal{X}_m$ for which the left side of eq. (50) can be non-zero, which yields eq. (48) and therefore the claim.

It remains to show that more than $|\mathcal{X}_m| - J'_m$ points p satisfy eq. (52) for large enough m . To see this, first define $(R'_m)_{m=1}^\infty \subset \mathbb{R}_+$ with

$$R'_m := \sqrt[d]{\frac{\text{vol}(\mathcal{M})}{\omega_d} \frac{J'_m}{|\mathcal{X}_m|}}, \quad (53)$$

as in lemma 4.3 and note that

$$\begin{aligned} \frac{\gamma}{J'_m |\mathcal{X}_m|^\eta} &\stackrel{\text{eq. (47)}}{\leq} \frac{\gamma}{J_0 |\mathcal{X}_m|^{\frac{2-d\eta}{d+2}} |\mathcal{X}_m|^\eta} = \frac{\gamma}{J_0 |\mathcal{X}_m|^{\frac{2+2\eta}{d+2}}} \\ &= \frac{\gamma}{J_0} \left(\frac{\omega_d}{J_0 \text{vol}(\mathcal{M})} \right)^{\frac{2}{d}} \left(\frac{J_0 \text{vol}(\mathcal{M})}{\omega_d} \right)^{\frac{2}{d}} |\mathcal{X}_m|^{-\frac{2+2\eta}{d+2}} \\ &= \frac{\gamma}{J_0} \left(\frac{\omega_d}{J_0 \text{vol}(\mathcal{M})} \right)^{\frac{2}{d}} \left(\frac{\text{vol}(\mathcal{M})}{\omega_d} \frac{J_0 |\mathcal{X}_m|^{\frac{2-d\eta}{d+2}}}{|\mathcal{X}_m|} \right)^{\frac{2}{d}} \\ &\stackrel{\text{eq. (53)}}{\leq} \frac{\gamma}{J_0} \left(\frac{\omega_d}{J_0 \text{vol}(\mathcal{M})} \right)^{\frac{2}{d}} (R'_m)^2 \stackrel{\text{eq. (19)}}{=} \frac{\sqrt[d]{\det(\text{Hess}_{p^*} F)}}{2(d+2)} (R'_m)^2. \quad (54) \end{aligned}$$

Here, the bound on η in the last estimate comes from the assumption in the theorem. Combining eq. (52) and eq. (54), we see that any point $p \in \mathcal{X}_m$ that satisfies

$$F(p) - \frac{1}{J'_m} \sum_{j=1}^{J'_m} F(p_{(j)}^m) \geq \frac{\sqrt[d]{\det(\text{Hess}_{p^*} F)}}{2(d+2)} (R'_m)^2. \quad (55)$$

also satisfies eq. (52). We now fix $0 < \epsilon < 1/2$ and consider the inequality

$$\lim_{m \rightarrow \infty} \frac{F(p) - \frac{1}{J'_m} \sum_{j=1}^{J'_m} F(p_{(j)}^m)}{(R'_m)^2} \geq (1 + \epsilon) \frac{\sqrt[d]{\det(\text{Hess}_{p^*} F)}}{2(d+2)}. \quad (56)$$

Then there exists an m' such that for all $m \geq m'$ too many points $p \in \mathcal{X}_m$ satisfy eq. (55) – and through eq. (52) also eq. (48) –, which yields our claim. The remainder of step (i-a) is devoted to showing that asymptotically too many $p \in \mathcal{X}_m$ satisfy eq. (56).

Consider the smaller ellipsoid $\mathcal{E}_{r'_m}^Q(p^*)$, again with $Q := \text{Hess}_{p^*} F$, but with smaller radius $r'_m := \sqrt{\frac{d+1+\epsilon}{d+2}} R'_m$. We will show that all points $p \in \mathcal{X}_m$ outside of $\mathcal{E}_{r'_m}^Q(p^*)$ asymptotically satisfy eq. (56). Then,

$$J'_m > |\mathcal{E}_{r'_m}^Q(p^*) \cap \mathcal{X}_m| \quad (57)$$

holds by eq. (39) in lemma 4.3, which yields the claim.

For showing that for large m all points outside of the ellipsoid $\mathcal{E}_{r'_m}^Q(p^*)$ satisfy eq. (56), it suffices to show that the inequality eq. (56) holds on the boundary $\partial \mathcal{E}_{r'_m}^Q(p^*)$. Indeed, since the function F has a unique minimiser, the family of ellipsoids $\mathcal{E}_r^Q(p^*)$ approximates a level sets of F for r small enough. Then, because $r'_m \rightarrow 0$ for large enough m the points in the sampling set \mathcal{X}_m outside $\mathcal{E}_{r'_m}^Q(p^*)$ must have a larger value of F than any element of the boundary $\partial \mathcal{E}_{r'_m}^Q(p^*)$, which implies that these points must have a zero-valued coefficient.

So, let $p \in \partial \mathcal{E}_{r'_m}^Q(p^*)$, i.e., we have

$$\text{Hess}_{p^*} F(\log_{p^*}(p), \log_{p^*}(p)) \stackrel{eq. (21)}{=} \sqrt[d]{\det(\text{Hess}_{p^*} F)} (r'_m)^2 = \sqrt[d]{\det(\text{Hess}_{p^*} F)} \frac{d+1+\epsilon}{d+2} (R'_m)^2. \quad (58)$$

Then we have

$$\begin{aligned} \lim_{m \rightarrow \infty} \frac{F(p) - \frac{1}{J'_m} \sum_{j=1}^{J'_m} F(p_{(j)}^m)}{(R'_m)^2} &= \lim_{m \rightarrow \infty} \frac{F(p) - \frac{1}{J'_m} \sum_{q \in \mathcal{E}_{R'_m}^Q(p^*) \cap \mathcal{X}_m} F(q)}{(R'_m)^2} \\ &= \lim_{m \rightarrow \infty} \frac{F(p) - F(p^*) - \frac{1}{J'_m} \left(\sum_{q \in \mathcal{E}_{R'_m}^Q(p^*) \cap \mathcal{X}_m} F(q) - F(p^*) \right)}{(R'_m)^2}, \quad (59) \end{aligned}$$

where we use the equality in eq. (39) to see that

$$\sum_{j=1}^{J'_m} F(p_{(j)}^m) = \sum_{q \in \mathcal{E}_{R'_m}^Q(p^*) \cap \mathcal{X}_m} F(q) \quad \text{holds since } p_{(j)}^m \text{ are points with minimal } F\text{-value.}$$

Then we can use Taylor expansion [15, (5.28)] and the fact that $dF(X) = 0$ for all $X \in \mathcal{T}_{p^*} \mathcal{M}$ by first-order optimality conditions to approximate the terms in the numerator:

$$\begin{aligned} F(p) - F(p^*) &= \frac{1}{2} \text{Hess}_{p^*} F(\log_{p^*}(p), \log_{p^*}(p)) + \mathcal{O}((r'_m)^3) \\ &\stackrel{eq. (21)}{=} \frac{1}{2} \sqrt[d]{\det(\text{Hess}_{p^*} F)} \frac{d+1+\epsilon}{d+2} (R'_m)^2 + \mathcal{O}((R'_m)^3), \quad (60) \end{aligned}$$

and for large m

$$\begin{aligned} &\frac{1}{J'_m} \sum_{q \in \mathcal{E}_{R'_m}^Q(p^*) \cap \mathcal{X}_m} (F(q) - F(p^*)) \\ &= \frac{1}{J'_m} \sum_{q \in \mathcal{E}_{R'_m}^Q(p^*) \cap \mathcal{X}_m} \left(\frac{1}{2} \text{Hess}_{p^*} F(\log_{p^*}(q), \log_{p^*}(q)) + \mathcal{O}((R'_m)^3) \right) \\ &\stackrel{eq. (39)}{=} \frac{1}{|\mathcal{E}_{R'_m}^Q(p^*) \cap \mathcal{X}_m|} \sum_{q \in \mathcal{E}_{R'_m}^Q(p^*) \cap \mathcal{X}_m} \left(\frac{1}{2} \text{Hess}_{p^*} F(\log_{p^*}(q), \log_{p^*}(q)) + \mathcal{O}((R'_m)^3) \right) \\ &= \frac{|\mathcal{X}_m|}{|\mathcal{E}_{R'_m}^Q(p^*) \cap \mathcal{X}_m|} \sum_{q \in \mathcal{E}_{R'_m}^Q(p^*) \cap \mathcal{X}_m} \frac{\left(\frac{1}{2} \text{Hess}_{p^*} F(\log_{p^*}(q), \log_{p^*}(q)) + \mathcal{O}((R'_m)^3) \right)}{|\mathcal{X}_m|} \\ &\stackrel{eq. (22)}{=} \frac{\text{vol}(\mathcal{M})}{\text{vol}(\mathcal{E}_{R'_m}^Q(p^*)) + \mathcal{O}((R'_m)^{d+1})} \sum_{q \in \mathcal{E}_{R'_m}^Q(p^*) \cap \mathcal{X}_m} \frac{\left(\frac{1}{2} \text{Hess}_{p^*} F(\log_{p^*}(q), \log_{p^*}(q)) + \mathcal{O}((R'_m)^3) \right)}{|\mathcal{X}_m|} \\ &\stackrel{eq. (23)}{=} \frac{1}{\text{vol}(\mathcal{E}_{R'_m}^Q(p^*)) + \mathcal{O}((R'_m)^{d+1})} \int_{\mathcal{E}_{R'_m}^Q(p^*)} \left[\frac{1}{2} \text{Hess}_{p^*} F(\log_{p^*}(q), \log_{p^*}(q)) + \mathcal{O}((R'_m)^3) \right] dq \end{aligned}$$

$$\begin{aligned}
&\stackrel{\text{eq. (34)}}{=} \frac{1}{2} \frac{\sqrt[d]{\det(\text{Hess}_{p^*} F)} \frac{\omega_d d}{d+2} (R'_m)^{d+2} + \mathcal{O}((R'_m)^{d+3})}{\omega_d (R'_m)^d + \mathcal{O}((R'_m)^{d+1})} \\
&= \frac{1}{2} \sqrt[d]{\det(\text{Hess}_{p^*} F)} \frac{d}{d+2} (R'_m)^2 + \mathcal{O}((R'_m)^3). \quad (61)
\end{aligned}$$

Bringing together the above results yields the validity of eq. (56)

$$\begin{aligned}
&\lim_{m \rightarrow \infty} \frac{F(p) - \frac{1}{J'_m} \sum_{j=1}^{J'_m} F(p_{(j)}^m)}{(R'_m)^2} \\
&= \lim_{m \rightarrow \infty} \frac{1}{2} \frac{\sqrt[d]{\det(\text{Hess}_{p^*} F)} \frac{d+1+\epsilon}{d+2} (R'_m)^2 - \sqrt[d]{\det(\text{Hess}_{p^*} F)} \frac{d}{d+2} (R'_m)^2 + \mathcal{O}((R'_m)^3)}{(R'_m)^2} \\
&= (1 + \epsilon) \frac{\sqrt[d]{\det(\text{Hess}_{p^*} F)}}{2(d+2)}, \quad (62)
\end{aligned}$$

and for large, but finite m still too many points must satisfy eq. (55) and hence eq. (48) follows, which gives our contradiction. We conclude that $J_m < J'_m$ for large enough m . Subsequently, we can drop the ceil operation, which gives the bound in eq. (25).

(i-b) Our claim that the points with non-zero coefficients lie in the ellipsoid – as stated in the theorem – also follows by realising that the upper bound from (i-a) gives us that the points with non-zero coefficients fit in $\mathcal{E}_{R_m}^Q(p^*)$ and by a similar level-set argument as above it must be that these points indeed live in this ellipsoid for large enough m .

(ii) For the lower bound in eq. (25) we will show that $\|\beta_m^*\|_0 > J''_m$, where

$$J''_m := \lfloor 3^{-\frac{d}{d+2}} J_0 |\mathcal{X}_m|^{\frac{2-d\eta}{d+2}} \rfloor. \quad (63)$$

In particular – and similarly to step (i-a) –, we will assume that $\|\beta_m^*\|_0 \leq J''_m$ but show that, for large m ,

$$\|(-\frac{|\mathcal{X}_m|^\eta}{\gamma} F_{\mathcal{X}_m} - \frac{1}{J''_m} \left(\sum_{j=1}^{J''_m} -\frac{|\mathcal{X}_m|^\eta}{\gamma} F(p_{(j)}^m) \right) + \frac{1}{J''_m})_+\|_0 > J''_m \quad (64)$$

holds. Then, also

$$\|(-\frac{|\mathcal{X}_m|^\eta}{\gamma} F_{\mathcal{X}_m} - \frac{1}{J''_m} \left(\sum_{j=1}^{J''_m} -\frac{|\mathcal{X}_m|^\eta}{\gamma} F(p_{(j)}^m) \right) + \frac{1}{J''_m})_+\|_0 > \|\beta_m^*\|_0 \quad (65)$$

holds by assumption. However, the latter is equivalent to $\|\beta_m^*\|_0 > J''_m$ by remark 3.2, which yields our contradiction. The remainder of (ii) is showing eq. (64).

If for any point $p \in \mathcal{X}_m$

$$\left(-\frac{|\mathcal{X}_m|^\eta}{\gamma} F(p) - \frac{1}{J''_m} \left(\sum_{j=1}^{J''_m} -\frac{|\mathcal{X}_m|^\eta}{\gamma} F(p_{(j)}^m) \right) + \frac{1}{J''_m} \right)_+ > 0 \quad (66)$$

holds, then

$$\left(-\frac{|\mathcal{X}_m|^\eta}{\gamma} F(p) - \frac{1}{J''_m} \left(\sum_{j=1}^{J''_m} -\frac{|\mathcal{X}_m|^\eta}{\gamma} F(p_{(j)}^m) \right) + \frac{1}{J''_m} \right)_+ > 0 \quad (67)$$

or equivalently

$$F(p) - \frac{1}{J_m''} \sum_{j=1}^{J_m''} F(p_{(j)}^m) < \frac{\gamma}{J_m'' |\mathcal{X}_m|^\eta}. \quad (68)$$

Similarly to step (i), we will show that too many points – that is more than J_m' – satisfy an even stronger inequality. For that, first define $(R_m'')_{m=1}^\infty \subset \mathbb{R}_+$ with

$$R_m'' := \sqrt[d]{\frac{\text{vol}(\mathcal{M})}{\omega_d} \frac{J_m''}{|\mathcal{X}_m|}}, \quad (69)$$

as in lemma 4.3 and – analogously to eq. (54) – note that

$$\begin{aligned} \frac{\gamma}{J_m'' |\mathcal{X}_m|^\eta} &\stackrel{\text{eq. (63)}}{\geq} \frac{\gamma}{3^{-\frac{d}{d+2}} J_0 |\mathcal{X}_m|^{\frac{2-d\eta}{d+2}} |\mathcal{X}_m|^\eta} = \frac{\gamma}{3^{-\frac{d}{d+2}} J_0 |\mathcal{X}_m|^{\frac{2+2\eta}{d+2}}} \\ &= \frac{\gamma}{3^{-\frac{d}{d+2}} J_0} \left(\frac{\omega_d}{3^{-\frac{d}{d+2}} J_0 \text{vol}(\mathcal{M})} \right)^{\frac{2}{d}} \left(\frac{3^{-\frac{d}{d+2}} J_0 \text{vol}(\mathcal{M})}{\omega_d} \right)^{\frac{2}{d}} |\mathcal{X}_m|^{-\frac{2+2\eta}{d+2}} \\ &= \frac{\gamma}{3^{-\frac{d}{d+2}} J_0} \left(\frac{\omega_d}{3^{-\frac{d}{d+2}} J_0 \text{vol}(\mathcal{M})} \right)^{\frac{2}{d}} \left(\frac{\text{vol}(\mathcal{M})}{\omega_d} \frac{3^{-\frac{d}{d+2}} J_0 |\mathcal{X}_m|^{\frac{2-d\eta}{d+2}}}{|\mathcal{X}_m|} \right)^{\frac{2}{d}} \\ &\stackrel{\text{eq. (69)}}{\geq} \frac{\gamma}{3^{-\frac{d}{d+2}} J_0} \left(\frac{\omega_d}{3^{-\frac{d}{d+2}} J_0 \text{vol}(\mathcal{M})} \right)^{\frac{2}{d}} (R_m'')^2 \stackrel{\text{eq. (19)}}{=} 3 \frac{\sqrt[d]{\det(\text{Hess}_{p^*} F)}}{2(d+2)} (R_m'')^2. \quad (70) \end{aligned}$$

Hence, for $p \in \mathcal{X}_m$ eq. (64) holds if

$$F(p) - \frac{1}{J_m''} \sum_{j=1}^{J_m''} F(p_{(j)}^m) < 3 \frac{\sqrt[d]{\det(\text{Hess}_{p^*} F)}}{2(d+2)} (R_m'')^2. \quad (71)$$

Next, fix $0 < \epsilon < 1/2$. Then, by a truncation argument it suffices to consider the asymptotic validity of the yet stronger inequality

$$\lim_{m \rightarrow \infty} \frac{F(p) - \frac{1}{J_m''} \sum_{j=1}^{J_m''} F(p_{(j)}^m)}{(R_m'')^2} \leq (3 - \epsilon) \frac{\sqrt[d]{\det(\text{Hess}_{p^*} F)}}{2(d+2)}, \quad (72)$$

Then for large m it still holds that too many points satisfy eq. (71) – and through eq. (68) also eq. (64) –, which yields our claim. The remainder of step (ii) is devoted to showing that asymptotically too many $p \in \mathcal{X}_m$ satisfy eq. (72).

Consider the ellipsoid $\mathcal{E}_{r_m'}^Q(p^*)$, again with $Q := \text{Hess}_{p^*} F$, but with $r_m' := \sqrt{\frac{d+1+\epsilon}{d+2}} R_m'$. We will show that all points $p \in \mathcal{X}_m$ outside of $\mathcal{E}_{r_m'}^Q(p^*)$ asymptotically satisfy eq. (72). Then,

$$J_m'' < |\mathcal{E}_{r_m'}^Q(p^*) \cap \mathcal{X}_m| \quad (73)$$

holds by eq. (40) in lemma 4.3, which yields the claim.

For showing that for large m all points outside of the ellipsoid $\mathcal{E}_{r_m'}^Q(p^*)$ satisfy eq. (72), it suffices to show to show that the inequality eq. (72) holds for all points on the boundary

$\partial \mathcal{E}_{r_m''}^Q(p^*)$. Indeed, by a similar line of reasoning as in step (i-a) the points with the lowest F -value will live in this ellipsoid.

So, let $p \in \partial \mathcal{E}_{r_m''}^F(p^*)$, i.e., we have

$$\text{Hess}_{p^*} F(\log_{p^*}(p), \log_{p^*}(p)) \stackrel{eq. (21)}{=} \sqrt[d]{\det(\text{Hess}_{p^*} F)} (r_m'')^2 = \sqrt[d]{\det(\text{Hess}_{p^*} F)} \frac{d+3-\epsilon}{d+2} (R_m'')^2. \quad (74)$$

Then, we have

$$\begin{aligned} & \lim_{m \rightarrow \infty} \frac{F(p) - \frac{1}{J_m''} \sum_{j=1}^{J_m''} F(p_{(j)}^m)}{(R_m'')^2} \\ &= \lim_{m \rightarrow \infty} \frac{1}{2} \frac{\sqrt[d]{\det(\text{Hess}_{p^*} F)} \frac{d+3-\epsilon}{d+2} (R_m'')^2 - \sqrt[d]{\det(\text{Hess}_{p^*} F)} \frac{d}{d+2} (R_m'')^2 + \mathcal{O}((R_m'')^3)}{(R_m'')^2} \\ &= (3-\epsilon) \frac{\sqrt[d]{\det(\text{Hess}_{p^*} F)}}{2(d+2)}, \quad (75) \end{aligned}$$

where the second term in the second line can be obtained in a similar fashion as done in eq. (61). Finally, for large, but finite m still too many points must satisfy eq. (71) and hence eq. (64) follows, which gives our contradiction. We conclude that $J_m > J_m''$ for large enough m . Subsequently, we can drop the floor operation, which gives the bound in eq. (25). \square

4.3 Well-posedness and consistency of the Riemannian barycentre

For proving theorem 3.7 we will argue that the error is fully determined by the choice of measure and moreover, that is sufficient to bound the error made by the measure. To make this more concrete, the lemma below expresses the distance between any point p^* , e.g., a minimiser of function on \mathcal{M} , and a solution p_μ^* to the lifted problem eq. (7) in terms of the Wasserstein distance between a point mass at p^* and the corresponding measure solving eq. (6).

Lemma 4.4. *Let \mathcal{M} be a connected Riemannian manifold, let $p^* \in \mathcal{M}$ and let $\mu \in \mathbb{P}_2(\mathcal{M})$ be a measure with support on a geodesically connected subset of \mathcal{M} . Then,*

$$d_{\mathcal{M}}(p_\mu^*, p^*) \leq 2W_2(\mu, \delta_{p^*}) \quad \text{for all } p_\mu^* \in P(\mu) \subset \mathcal{M} \quad (76)$$

where the (possibly set-valued) solution operator mapping $P: \mathbb{P}_2(\mathcal{M}) \rightrightarrows \mathcal{M}$ is defined as in eq. (7).

Proof. First, note that for all $p \in \mathcal{M}$

$$W_2(\mu, \delta_p)^2 = \inf_{\pi \in \Gamma(\mu, \delta_p)} \int_{\mathcal{M} \times \mathcal{M}} d_{\mathcal{M}}(q, q')^2 d\pi(q, q') = \int_{\mathcal{M}} d_{\mathcal{M}}(q, p)^2 d\mu(q), \quad (77)$$

as every coupling π with marginals μ and δ_p must satisfy $\pi = \mu \otimes \delta_p$.

Next, p_μ^* exists since μ has support on a geodesically connected subset and we have $W_2(\mu, \delta_{p_\mu^*}) \leq W_2(\mu, \delta_{p^*})$, since

$$\begin{aligned} W_2(\mu, \delta_{p_\mu^*})^2 &= \int_{\mathcal{M}} d_{\mathcal{M}}(q, p_\mu^*)^2 d\mu(q) = \inf_{p \in \mathcal{M}} \int_{\mathcal{M}} d_{\mathcal{M}}(q, p)^2 d\mu(q) \\ &\leq \int_{\mathcal{M}} d_{\mathcal{M}}(q, p^*)^2 d\mu(q) = W_2(\mu, \delta_{p^*})^2. \end{aligned}$$

The claim now follows from fact that W_2 is satisfies the triangle inequality:

$$d_{\mathcal{M}}(p_{\mu}^*, p^*) = W_2(\delta_{p_{\mu}^*}, \delta_{p^*}) \leq W_2(\mu, \delta_{p_{\mu}^*}) + W_2(\mu, \delta_{p^*}) \leq 2W_2(\mu, \delta_{p^*}). \quad (78)$$

□

Lemma 4.4 shows that an analysis of the error rate that covers not only the convexification and projection errors, but also discretisation and relaxation errors can be based on bounds for the Wasserstein distance. Indeed, if the non-zero coefficients of β concentrate on a geodesically connected subset of \mathcal{M} and $W_2(\sum_{p \in \mathcal{X}} \beta_p^* \delta_p, \delta_{p^*})$ goes to 0 for large enough sampling sets, we obtain convergence of the result of the lifting approach $p_{\mathcal{X}}^*$ to the solution of the original problem, say p^* , as well.

Proof of theorem 3.7. Fix an η -local low-discrepancy sequence $(\mathcal{X}_m)_{m=1}^{\infty} \subset S(\mathcal{M})$. Define $(\beta_m^*)_{m=1}^{\infty} \subset \ell_0$ as the zero-padded solution operator of eq. (13), so it is given as

$$\beta_m^* := \left(\Pi_{\Delta|\mathcal{X}_m|} \left(-\frac{|\mathcal{X}_m|^{\eta}}{\gamma} F_{\mathcal{X}_m} \right), 0, \dots \right). \quad (79)$$

First, from the locality statement of theorem 3.6 – that is the points with non-zero coefficients being concentrated on an ellipsoid – existence of the barycentre generated by β_m^* for $m \geq m'$ holds on the submanifold $\mathcal{B}_{r_{m'}}(p^*) \subset \mathcal{M}$ that is the (geodesically convex) geodesic ball with radius $r_{m'}$ such that it is containing all the ellipsoids containing the support of β_m^* for $m \geq m'$ by [43, Proposition 1]. With the measures concentrated in $\mathcal{B}_{r_{m'}}(p^*)$ the uniqueness claim of the barycentre holds by the famous result by Kendall [39, Theorem 7.3]. This shows the first claim eq. (26).

Consequently, for the bound in the second claim eq. (27), $\mathbb{P}_2(\mathcal{B}_{r_{m'}}(p^*))$ is well-defined and from lemma 4.4 we obtain that it is sufficient to show

$$W_2 \left(\sum_{p \in \mathcal{X}_m} (\beta_m^*)_p \delta_p, \delta_{p^*} \right) \leq \sqrt{\frac{d \det(\text{Hess}_{p^*} F)}{\lambda_{\min}(\text{Hess}_{p^*} F)}} \sqrt[4]{J_0 \frac{\text{vol}(\mathcal{M})}{\omega_d} |\mathcal{X}_m|^{-\frac{1+\eta}{d+2}}}. \quad (80)$$

Indeed, if the above is established, the additional factor of 2 from the lemma gives the desired result.

So it remains to show eq. (80). For that, note that for large m , there must be less than $J_0 |\mathcal{X}_m|^{\frac{2-d\eta}{d+2}}$ points with non-zero coefficients by theorem 3.6. Additionally, these points lie in the ellipsoid $\mathcal{E}_{R_m}^Q(p^*)$ with $Q := \text{Hess}_{p^*} F$, whose size is defined by the radius $R_m \in \mathbb{R}_+$, defined in eq. (24), i.e.,

$$R_m := \sqrt[4]{J_0 \frac{\text{vol}(\mathcal{M})}{\omega_d} |\mathcal{X}_m|^{-\frac{1+\eta}{d+2}}}. \quad (81)$$

Then, taking into account that

$$d_{\mathcal{M}}(p, p^*)^2 \leq \frac{\sqrt{d \det(\text{Hess}_{p^*} F)}}{\lambda_{\min}(\text{Hess}_{p^*} F)} (R_m)^2 \quad \text{for } p \in \mathcal{E}_{R_m}^Q(p^*), \quad (82)$$

the bound on the Wasserstein distance follows directly, as for large m

$$\begin{aligned} W_2\left(\sum_{p \in \mathcal{X}_m} (\beta_m^*)_p \delta_p, \delta_{p^*}\right)^2 &= \sum_{p \in \mathcal{X}_m} (\beta_m^*)_p d_{\mathcal{M}}(p, p^*)^2 \stackrel{\text{theorem 3.6}}{\leq} \sum_{p \in \mathcal{E}_{R_m}^Q(p^*) \cap \mathcal{X}_m} (\beta_m^*)_p d_{\mathcal{M}}(p, p^*)^2 \\ &\stackrel{\text{eq. (82)}}{\leq} \sum_{p \in \mathcal{E}_{R_m}^Q(p^*) \cap \mathcal{X}} (\beta_m^*)_p \frac{\sqrt[2]{\det(\text{Hess}_{p^*} F)}}{\lambda_{\min}(\text{Hess}_{p^*} F)} (R_m)^2 \leq \frac{\sqrt[2]{\det(\text{Hess}_{p^*} F)}}{\lambda_{\min}(\text{Hess}_{p^*} F)} (R_m)^2, \end{aligned} \quad (83)$$

where the last equality follows from the fact that $\sum_{p \in \mathcal{X}_m} (\beta_m^*)_p = 1$. \square

Remark 4.5. From the proof above one could argue that the bound in eq. (27) is overly pessimistic. This observation mainly arises from the fact that the Wasserstein-2 distance does not take the effect of averaging into account, but only measures the effort of moving mass from one place to another. In particular, the bound suggests that more points with non-zero coefficients could do worse than collapsing into a single point.

At this stage the non-linear structure of the manifold makes it difficult to obtain a tighter bound that does take this effect into account. For now, we will leave it for future research and instead focus on gathering empirical evidence that the proposed method – in the non-collapsed regime – outperforms collapsing in section 7.

4.4 Approximating the regularisation parameter

Finally, it remains to show proposition 3.8. The proof relies heavily on the ideas developed in the proof of theorem 3.6.

Proof of proposition 3.8. Fix an η -local low-discrepancy sequence $(\mathcal{X}_m)_{m=1}^\infty \subset S(\mathcal{M})$ and define $(J_m)_{m=1}^\infty \subset \mathbb{N}$ by $J_m := \lfloor J_0 |\mathcal{X}_m|^{\frac{2-d\eta}{d+2}} \rfloor$ and $(R_m)_{m=1}^\infty \subset \mathbb{N}$ by $R_m := \sqrt[2]{\frac{\text{vol}(\mathcal{M})}{\omega_d} \frac{J_m}{|\mathcal{X}_m|}}$. Additionally, for any $m \in \mathbb{N}$ define the points $p_{(1)}^m, \dots, p_{(|\mathcal{X}_m|)}^m$ by labeling the elements of \mathcal{X}_m such that $F(p_{(1)}^m) \leq \dots \leq F(p_{(|\mathcal{X}_m|)}^m)$.

Choose $0 < \epsilon < 1/2$, define $r_m := \sqrt{\frac{d+2+\epsilon}{d+2}} R_m$ and let $p \in \partial \mathcal{E}_{r_m}^Q(p^*)$ with $Q := \text{Hess}_{p^*} F$. Then, analogously to the argument in theorem 3.6 we have

$$\begin{aligned} \lim_{m \rightarrow \infty} \frac{1}{2} \frac{F(p) - \frac{1}{J_m} \sum_{j=1}^{J_m} F(p_{(j)}^m)}{R_m^2} &= \lim_{m \rightarrow \infty} \frac{1}{4} \frac{\sqrt[2]{\det(\text{Hess}_{p^*} F)}^{\frac{d+2+\epsilon}{d+2}} R_m^2 - \sqrt[2]{\det(\text{Hess}_{p^*} F)}^{\frac{d}{d+2}} R_m^2 + \mathcal{O}(R_m^3)}{R_m^2} \\ &= \frac{2+\epsilon}{2} \frac{\sqrt[2]{\det(\text{Hess}_{p^*} F)}}{2(d+2)}, \end{aligned} \quad (84)$$

Since ϵ is arbitrary and $p_{(J_m+1)} \in \mathcal{E}_{r_m}^Q(p^*)$ for large enough m , but $p_{(J_m+1)} \notin \mathcal{E}_{R_m}^Q(p^*)$, we must have that $p_{(J_m+1)}$ gets arbitrarily close to the boundary $\partial \mathcal{E}_{R_m}^Q(p^*)$ as m grows, i.e.,

$$\lim_{m \rightarrow \infty} \frac{1}{2} \frac{F(p_{(J_m+1)}^m) - \frac{1}{J_m} \sum_{j=1}^{J_m} F(p_{(j)}^m)}{R_m^2} = \frac{\sqrt[2]{\det(\text{Hess}_{p^*} F)}}{2(d+2)}. \quad (85)$$

Multiplying both sides by $J_0^{\frac{d+2}{d}} \left(\frac{\text{vol}(\mathcal{M})}{\omega_d} \right)^{\frac{2}{d}}$ and substituting the definition of R_m now gives the desired result. □

5 Single particle Cryo-EM

This section provides a brief overview of the inverse problem in single particle Cryo-EM. We start out by briefly describing the application area (section 5.1) and then shift focus to formulating the inverse problem mathematically (section 5.2). Emphasis here is on the case with homogeneous particles, which corresponds to joint 3D reconstruction and rotation estimation. The discussion is then centered around solving the joint recovery problem. That is, we discuss and review existing mathematical results and algorithms and consider the problem of noise-robustness versus data-consistency in performing joint recovery in this context (section 5.3).

5.1 Cryo-EM in structural biology

Biological macromolecules (or biomolecules), like proteins and nucleic acids, are critical in biological processes that sustain both life and disease. Their structure (3D ‘shape’) along with its dynamics plays a key role in understanding their function in specific biochemical reactions. Much attention has therefore been devoted to methods for determining such structures and their dynamics and much of structural biology focuses on this.

Historically, protein structures are computationally determined from X-ray crystallography data. This involves solving a challenging inverse problem and both experimental and algorithmic progress in the field has been extremely successful, thus turning X-ray crystallography into a standard method in structural biology for structure recovery of biomolecules. However, an inherent drawback with X-ray crystallography is that the approach is by design restricted to studying structures of biomolecules in crystalline state, thus making it difficult to uncover conformational dynamics. The technique is also not possible to use on biomolecules, such as membrane proteins, that are difficult, if not impossible, to crystallise. In contrast, cryogenic electron microscopy (Cryo-EM) opens up for the possibility to study biomolecules in their native aqueous environment. The field has made rapid advances in the last few years regarding both sample preparation, instrumentation and computational methods. This development was recognised through the 2017 Nobel Prize in Chemistry.

Single particle Cryo-EM is a specific Cryo-EM technique that uses principles from tomography to computationally determine the 3D structure of a biomolecule and potentially also uncover the multiple states representing its dynamics. The starting point is to prepare an aqueous solution that contains a large number of copies of the biomolecule to be studied, where each copy is referred to as a *particle*. Next, cryofixation is applied to this solution, resulting in a thin slab of vitrified ice that contains these particles. The slab is then imaged in a high-resolution transmission electron microscope (TEM) resulting in several 2D phase contrast images (micrographs). Next, image processing techniques are used to extract several 2D image patches from each micrograph. Each such patch represents a noisy 2D “projection image” of a *single* particle in an unknown pose, the latter encoding its 3D rotation and 2D in-plane translation w.r.t. a common 3D reference. The aim is now to computationally recover a volumetric representation of the 3D structure of the biomolecule (3D map) from these aforementioned 2D image patches.

It is clearly not possible to independently recover a 3D map of each particle from the corresponding single 2D image patch that is a “projection image” of the former. Therefore, a key

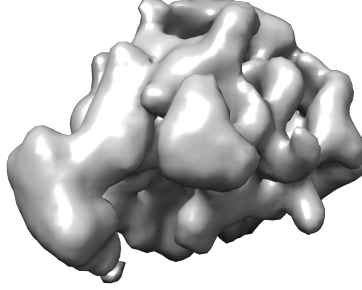


Figure 1: Surface rendering of a 3D map for a particle representing the 70S ribosomal subunit.

assumption in single particle Cryo-EM is that *all* particles are copies of the *same biomolecule*. This assumption is then used in mathematical techniques from tomography to recover a 3D map of the biomolecule from the aforementioned 2D image patches. An important case is when the biomolecule is rigid (homogeneous particles). Then, all particles can be assumed to have (approximately) identical 3D maps and the 2D image patches represent tomographic data of a single 3D object. In that setting, once particle specific poses are determined, it is possible to use standard mathematical techniques from tomography to recover the 3D map from the 2D image patches. A more challenging case is when the biomolecule is flexible (heterogeneous particles). The goal is now to recover a dynamical 3D map from the 2D image patches, which is significantly more challenging.

Finally, a recovered 3D map is a volumetric representation of the 3D electrostatic potential generated by the biomolecule and the surrounding aqueous buffer. This 3D map can in principle be used to determine the exact location of each atom in the biomolecule, i.e., its 3D atomic model [49, 16].

5.2 Mathematical formalisation of structure recovery in Cryo-EM

The aim here is to phrase structure recovery in single particle Cryo-EM as an inverse problem.

3D maps and 2D image patches A 3D map of a particle can mathematically be represented by a scalar field $u: \mathbb{R}^3 \rightarrow \mathbb{R}$ that encodes the 3D distribution of the electrostatic potential generated by the particle embedded in vitrified aqueous buffer. An example of such a 3D map is shown in fig. 1. Henceforth, \mathcal{X} denotes the Hilbert space of real-valued functions on \mathbb{R}^3 that can be the 3D map for some biomolecule, see [50, p. 952] for more on how to characterise such a function space. Similarly, measured data representing a 2D image patch can be formally seen as noisy samples of a function $f: \mathbb{R}^2 \rightarrow \mathbb{R}$ on the TEM detector plane. Here, \mathcal{Y} is a Hilbert space of real-valued functions on \mathbb{R}^2 that can be Cryo-EM noise-free continuum data of a biomolecule.

The inverse problem The aim in single particle Cryo-EM to reconstruct the 3D structure of a biomolecule from single particle data. Assuming homogeneous particles, one can formalise this as the task of recovering a 3D map $u \in \mathcal{X}$ from 2D projection images $f_1, \dots, f_N \in \mathcal{Y}$. Here, each $f_i \in \mathcal{Y}$ is a single sample of the \mathcal{Y} -valued random variable \mathbb{f}_i where

$$\mathbb{f}_i = \mathcal{A}(g_i.u) + \mathbb{e}_i \quad \text{with } g_i \in \text{SO}(3) \text{ and } \mathbb{e}_i \sim \text{P}_{\text{noise}}^i \text{ for } i = 1, \dots, N. \quad (86)$$

The inverse problem is the task of *jointly* recovering the 3D map $u \in \mathcal{X}$ of the biomolecule while estimating (or marginalising out) the unknown particle specific 3D rotations $g_i \in \text{SO}(3)$ for $i = 1, \dots, N$.

The operator $\mathcal{A}: \mathcal{X} \rightarrow \mathcal{Y}$ (*forward operator*) in eq. (86) is assumed to be known and it associates a 3D map $u: \mathbb{R}^3 \rightarrow \mathbb{R}$ to a 2D image patch $f: \mathbb{R}^2 \rightarrow \mathbb{R}$. It is a mathematical model for image formation in a high resolution TEM in the sense that it simulates the 2D image data obtained in absence of noise from a particle with a given 3D map. See below for an explicit expression for this operator. Next, $\mathbf{P}_{\text{noise}}^i$ denotes the statistical distribution for the \mathcal{Y} -valued random variable \mathbf{e}_i that represents the observation noise. Furthermore, each 3D rotation $g_i \in \text{SO}(3)$ acts on a 3D map according to the group action $g.u := u \circ g^{-1}$ for $g \in \text{SO}(3)$.

Remark 5.1. *The inverse problem based on eq. (86) represents a simplified setting that disregards in-plane translations and molecular symmetries. More precisely, eq. (86) assumes all particle specific 2D image patches are perfectly aligned. This is often not the case, meaning that there is an additional unknown in-plane translation $t_i \in \mathbb{R}^2$. Accounting for this translation means replacing $\text{SO}(3)$ in eq. (86) with $\text{SO}(3) \times \mathbb{R}^2$. Next, the biomolecule might also have certain known rotational symmetries [36] that are encoded by a group $G \subset \text{SO}(3)$. To account for this, one needs to consider 3D rotations in the quotient group $\text{SO}(3)/G$. In summary, the variant of eq. (86) that handles in-plane translations and molecular symmetries reads as*

$$\mathbf{f}_i = \mathcal{A}(g_i.u) + \mathbf{e}_i \quad \text{with } g_i \in (\text{SO}(3)/G) \times \mathbb{R}^2 \text{ and } \mathbf{e}_i \text{ as in eq. (86) for } i = 1, \dots, N. \quad (87)$$

The forward operator When imaging thin unstained cryofixed biological specimens in a high resolution TEM, one can assume that the weak-phase object approximation holds [74, 50]. This approximation allows us to express \mathcal{A} as a parallel beam ray transform on lines parallel to the TEM optical axis (tomographic projection) followed by a 2D convolution in the detector plane to account for TEM optics and detector response [50].

Phrasing the above mathematically, we get that $\mathcal{A}: \mathcal{X} \rightarrow \mathcal{Y}$ in eq. (86) is of the form

$$\mathcal{A}(u) := H * (\mathcal{P}(u)) \quad \text{for } u \in \mathcal{X}. \quad (88)$$

In the above, $\mathcal{P}: \mathcal{X} \rightarrow \mathcal{Y}$ is the parallel beam ray transform (projection mapping) restricted to lines parallel to the TEM optical axis. Choosing a coordinate system where the z -axis is parallel to the TEM optical axis allows us to express it as

$$\mathcal{P}u(x, y) := \int_{-\infty}^{\infty} u(x, y, z) dz. \quad (89)$$

Next, the convolution in eq. (88) is a 2D convolution in the detector plane and the corresponding convolution kernel $H: \mathbb{R}^2 \rightarrow \mathbb{R}$ is given analytically by its Fourier transform:

$$\hat{H}(\xi) := -A(\xi) \left(\sqrt{1 - \alpha^2} \sin(W(|\xi|)) + \alpha \cos(W(|\xi|)) \right) \quad (90)$$

with $0 < \alpha < 1$ denoting the *amplitude contrast ratio*, $A: \mathbb{R}^2 \rightarrow \mathbb{R}$ is the aperture function that is commonly an indicator function on a disc with a radii given by the TEM objective aperture, and

$$W(s) := \frac{\Delta z}{2k} s^2 - \frac{C_s}{4k^3} s^4$$

models imperfections in the TEM optics. Here, Δz is the *defocus*, C_s is the *spherical aberration*, and k is the (relativistically corrected) *wave number* of the imaging electron. The function \hat{H} in eq. (90) is often referred to as the *contrast transfer function* (CTF).

5.3 Survey of reconstruction methods for single particle Cryo-EM

Mathematically, the first natural question that comes to mind when analysing an inverse problem is uniqueness. For tomographic imaging problems this typically means determining whether uniqueness holds assuming continuum noise-free data generated by a perfectly known forward operator. For eq. (86), this means to determine whether uniqueness holds for the joint problem of recovering the 3D map and estimating the particle specific 3D rotations. When the forward operator \mathcal{A} in eq. (86) is the parallel beam ray transform, then one can, except for some special cases, prove uniqueness up to a global orthogonal transformation [42]. Interestingly, adopting a more realistic TEM imaging model (based on Born approximation and TEM optics) allows one to prove uniqueness without any global orthogonal transformation [41].

The next natural mathematical topic is to characterise the degree of ill-posedness of the inverse problem in eq. (86). If particle specific 3D rotations are known, then eq. (86) reduces to inverting the parallel beam ray transform on complete data (actually data is here the entire 4D manifold of lines, so the problem is over-determined), which is known to be a mildly ill-posed problem. As to be expected, the ill-posedness worsens when 3D rotations are also unknown. Even though the authors are unaware of any mathematically rigorous characterisations of the degree of ill-posedness in this setting, numerical experience strongly suggests that the inverse problem in eq. (86) is severely ill-posed.

The above theoretical issues represent a small part of the research within computational sciences inspired by single particle Cryo-EM. The main focus within the Cryo-EM community has been on the design and implementation of algorithms for solving eq. (86). This inverse problem amounts to jointly solving two coupled inverse problems, namely one related to recovering the 3D map and the other on recovering particle specific 3D rotations. These two inverse problems, which are coupled in eq. (86), have very different characteristics. Hence, it was natural to seek methods that “disentangle” them.

Early approaches relied on the observation that if the forward model is the parallel beam ray transform, then one can use integral geometric techniques to estimate 3D rotations without having access to a 3D map. With this disentanglement, one can first estimate particle specific 3D rotations, then use these to recover the 3D map. Such an approach was suggested as early as 1986 [69] for retrieving relative rotations of 2D projections in Fourier space through common lines. Soon after, the method of moments [26, 27, 28, 56] was proposed and later further improved and analyzed in [6, 7], which did not need any information on the 3D map either. A different – by now famous – statistical approach is Kam’s auto-correlation analysis, which dates back to 1980 [37]. Here, the recovery of the 3D map bypasses the estimation of the rotations. Instead, the recovery of the 3D map is based on using the 2D image patches to compute the autocorrelation and higher order correlation functions of the 3D map in Fourier space.

One limitation with many of the above methods relates to difficulties in handling the high noise levels present in contemporary low-dose single particle Cryo-EM data. As an example, the method of moments breaks down under such high noise conditions, and it has shown to be difficult to make it more robust against noise. The common lines method on the other hand – although also breaking down under high noise in the standard form – has had several extensions that have turned out to be more resilient to noise than the original common lines method [4, 60, 62, 63, 75]. Similarly to the common lines method, Kam’s method has also served as an inspiration for several extensions [13, 3, 46, 59].

Apart from noise, a second hurdle relates to the forward operator, and in particular to the varying CTF between micrographs. For this reason and other factors such as structural heterogeneity of particles, there is typically a refinement stage after the *ab initio* phase as described above. The brief survey here focuses on the current state-of-the-art methods and

these are typically based on variational models of the type

$$\inf_{\substack{u \in \mathcal{X} \\ g_1, \dots, g_N \in \text{SO}(3)}} \left\{ \sum_{i=1}^N \left[\mathcal{L}(\mathcal{A}_i(g_i \cdot u), f_i) \right] + \mathcal{R}(u) \right\}. \quad (91)$$

Here, $\mathcal{R}: \mathcal{X} \rightarrow \mathbb{R}$ is a suitably chosen (often convex) regularisation functional whereas $\mathcal{L}: \mathcal{Y} \times \mathcal{Y} \rightarrow \mathbb{R}$ quantifies similarity in data space \mathcal{Y} . One may choose the latter as an appropriate affine transformation of the negative log-likelihood for data. The precise expression can be derived from knowledge about $\mathbf{e}_i \sim \mathbf{P}_{\text{noise}}^i$ in eq. (86). Then, minimising $u \mapsto \mathcal{L}(\mathcal{A}(g \cdot u), f)$ amounts to computing a maximum likelihood estimation given data $f \in \mathcal{Y}$ and 3D rotation $g \in \text{SO}(3)$. A typical assumption is that \mathbf{e}_i are independent and (approximately) Gaussian distributed with zero mean and variance $\sigma > 0$ (noise level in data). Then

$$\mathcal{L}(f, f') = \frac{1}{2\sigma} \|f - f'\|_{\mathcal{Y}}^2 \quad \text{for } f, f' \in \mathcal{Y} \text{ and noise level } \sigma > 0. \quad (92)$$

The minimisation in eq. (91) is typically solved through an iterative scheme where updates for the 3D map in \mathcal{X} are intertwined in an alternating manner with updates of the particle specific 3D rotations in $\text{SO}(3)$. Again, this corresponds to a kind of disentanglement and within such an approach, the variant of eq. (1) that corresponds to 3D rotation estimation only – i.e., eq. (91) assuming fixed known $u \in \mathcal{X}$ – is not the full problem. Solving it, however, is one of the central challenges the single particle Cryo-EM and the community has been devoting significant effort into this as we briefly survey. Note that these methods tend to utilise additional special structure of the objective in eq. (1) and the fact that $\mathcal{M} = \text{SO}(3)$. As such, they stand in contrast to research on manifold optimisation pursued within the mathematical community, where focus is on methods for solving general optimisation problems on manifolds with provable convergence guarantees.

Early work on iterative refinement can be traced back as early as 1972 [24] and to follow up works such as [34], where typically a 3D map update step alternated with an rotation alignment step. These type of algorithms were also the cornerstone of the first generation of software packages [23, 47, 70] and most software packages being released in the years after followed this approach [31, 35, 58, 65, 66].

Arguably, starting from the 2010 there has been a shift in rotation estimation in refinement, and there are now two packages dominating the field: RELION [57] and cryoSPARC [54]. Rather than picking one rotation after every alignment step – which can suffer from high noise levels – RELION gives probabilities to each rotation and marginalizes over a large set. Although technically solving a different problem now, this method tends to be very robust to noise because of this averaging approach. CryoSPARC on the other hand uses a branch-and-bound algorithm for the rotation estimation, which is more sophisticated than plain alignment and faster than the RELION approach. It also solves the original problem rather than a modification, but arguably pays in noise-robustness.

Even more recently, deep learning-based methods have been introduced to joint refinement. Here too approaches can be categorized by whether they work around the rotations through marginalisation [33] or try to actually find them through a multi-scale solver [79]. To summarise, model- or learning-based refinement methods proposed so far do not take full advantage of the manifold structure of $\text{SO}(3)$. This stands in contrast to the *ab initio* methods. In works where this is attempted [77], authors typically resort to local charts, which have the drawbacks outlined in section 1.1. As we next argue, there is plenty to be gained here.

6 Application of ESL to single particle Cryo-EM

In this section, we combine the ESL approach (algorithm 1) with a scheme for solving optimisation problems of the form eq. (91) with the loss in eq. (92) and a single forward operator for all 2D images. As outlined in section 6.1, this results in a computationally efficient scheme for joint 3D rotation estimation and 3D map reconstruction in single particle Cryo-EM that can be generalized straightforwardly into a proper refinement method, i.e., also taking into account in-plane shifts and varying TEM optics CTF across 2D image patches.

Subsequently, we will briefly provide some additional practical considerations by relating our method to other methods in a more heuristic fashion (section 6.2), with a focus on the trade-off between noise-robustness and data-consistency as mentioned in section 5.3.

6.1 Lifting-based rotation estimation by alternating minimisation

Let $\Omega \subset \mathbb{R}^3$ be a bounded domain and assume our 3D maps reside in the function space $L^2(\Omega)$. If one chooses a regularisation functional $\mathcal{R}: L^2(\Omega) \rightarrow \mathbb{R}$ as

$$\mathcal{R}(u) = \frac{1}{2\tau_1} \|u\|_2^2 + \frac{1}{2\tau_2} \|\mathcal{K} * u\|_2^2 \quad \text{for some } \tau_1, \tau_2 > 0, \quad (93)$$

where $\mathcal{K}: L^2(\Omega) \rightarrow L^2(\Omega)$ is a low-pass filter defined by its Fourier transform as $\widehat{\mathcal{K}}(\xi) := |\xi|$, then the joint 3D map reconstruction and rotation estimation problem eq. (91) with eq. (92) and a single forward operator for all 2D images reads as

$$\inf_{\substack{u \in L^2(\Omega) \\ g_1, \dots, g_N \in \text{SO}(3)}} \left\{ \sum_{i=1}^N \left[\frac{1}{2\sigma} \|\mathcal{A}(g_i \cdot u) - f_i\|_2^2 \right] + \frac{1}{2\tau_1} \|u\|_2^2 + \frac{1}{2\tau_2} \|\mathcal{K} * u\|_2^2 \right\} \quad (94)$$

for some noise level $\sigma > 0$. We propose to solve eq. (94) using the following alternating iterative scheme:

$$g_i^{k+1} := \underset{g \in \text{SO}(3)}{\operatorname{argmin}} \left\{ \frac{1}{2\sigma} \|\mathcal{A}(g \cdot u^k) - f_i\|_2^2 \right\} \quad \text{for } i = 1, \dots, N, \quad (95)$$

$$u^{k+1} := \underset{u \in L^2(\Omega)}{\operatorname{argmin}} \left\{ \sum_{i=1}^N \frac{1}{2\sigma} \|\mathcal{A}(g_i^{k+1} \cdot u) - f_i\|_2^2 + \frac{1}{2\tau_1} \|u\|_2^2 + \frac{1}{2\tau_2} \|\mathcal{K} * u\|_2^2 \right\}. \quad (96)$$

As already mentioned at the end of section 5.1, solving eq. (96) is typically straightforward. In the Cryo-EM setting, one can even express the solution in closed form – as will be discussed in the following. Hence, the challenging part lies in solving eq. (95) for the particle-specific 3D rotations under high noise conditions. This will be addressed using the developed machinery from the previous section. The resulting joint recovery algorithm is summarized in algorithm 2. Below we elaborate on several steps in the method and introduce the notation.

Initialisation First note that because of the non-convexity of eq. (94), proper initialisation of either the 3D map or the rotations will be key. *Ab initio* modelling has been developed to provide 3D maps u^0 [3, 4, 13, 46, 59, 60, 63, 75] and although in several instances initial estimates for the rotations are also provided, this is not always the case. Hence, we will assume there is no *a priori* information on rotations, i.e., we start the algorithm by estimating them.

Updating particle specific 3D rotations Key components for using ESL (algorithm 1) for estimating particle specific 3D rotations by solving eq. (95) is the choice of sampling set \mathcal{X} – or rather choice of initial set \mathcal{X}_0 and a refinement strategy – and the choices of the regularisation parameter $\gamma > 0$ and the scaling factor $\eta > 0$ in the regularised formulation eq. (13) of eq. (95).

In this work, \mathcal{X}_0 is obtained from a symmetric uniform mesh over \mathbb{S}^3 of size 3 642 whose uniformity has been verified numerically [76, Table 10]. Realising that \mathbb{S}^3 is a double cover of $\text{SO}(3)$ and that the two can be identified [29, Lemma 1], yields a sampling set $\mathcal{X}_0 \subset \text{SO}(3)$ with $|\mathcal{X}_0| = 1\,821$ and better uniformity – in terms of integration error – than mathematically derived sampling sets that are typically much smaller [30]. For generating larger sampling sets, a triangulation of \mathcal{X}_0 is constructed and midpoint refinement is used to construct 7 smaller simplices from each simplex in the triangulation [67, Fig. 2]. The procedure can be repeated until the desired mesh resolution is obtained. Section 7 investigates several meshes.

When choosing γ and η one should consider that the effect of the former can be compensated for by the latter and vice versa for a fixed sampling set – which is the case in a real-world scenario. Therefore, even though one could be tempted to pick η yielding the lowest bound in theorem 3.7, one should rather consider theorem 3.6 for picking η , i.e., prioritize on controlling the amount of non-zero coefficients in the sampling set. Nevertheless, here one also sees that choosing $\eta \approx 2/3$ will give most control, i.e., least variability between the upper and lower bound, and hence will also be the preferred choice from a practical point of view.

For γ , the approximation in proposition 3.8 is then used due to the unavailability of the Riemannian Hessian of the objective functions eq. (95) – note the bracket notation for the labeling of the rotations as in the proposition is also used in algorithm 2. Finally, section 7 investigates if one can actually choose η this high and if so, how many points with non-zero coefficients one needs for proper performance, i.e., how to pick J_0 in proposition 3.8.

Updating the 3D map For the 3D map update it is key to have an efficient algorithm for solving eq. (96) and properly chosen parameters σ , τ_1 and τ_2 .

Our 3D map update builds on the approach taken in RELION [57]. In particular, we extend the computationally efficient closed-form solution of the RELION 3D map update scheme with an additional regulariser of the form $u \mapsto \frac{1}{2\tau_2} \|\mathcal{K} * u\|_2^2$ term:

$$u^{k+1} := \underset{u \in L^2(\Omega)}{\operatorname{argmin}} \left\{ \sum_{i=1}^N \frac{1}{2\sigma} \|\mathcal{A}(g_i^{k+1} \cdot u) - f_i\|_2^2 + \frac{1}{2\tau_1} \|u\|_2^2 + \frac{1}{2\tau_2} \|\mathcal{K} * u\|_2^2 \right\} \quad (97)$$

$$= a^{k+1} * \left[\sum_{i=1}^N \frac{\tau_1}{\sigma} (g_i^{k+1})^{-1} \cdot \mathcal{A}^*(f_i) \right], \quad (98)$$

where a^{k+1} is defined by its Fourier transform as

$$\widehat{a}^{k+1} := \frac{1}{\sum_{i=1}^N \frac{\tau_1}{\sigma} ((g_i^{k+1})^{-1} \cdot \widehat{\mathcal{A}^*(H)}) + \frac{\tau_1}{\tau_2} \widehat{\mathcal{K}}^2 + 1} \quad \text{with } H \text{ as in eq. (90)}. \quad (99)$$

As shown above, the addition of the second regulariser does not complicate the numerical substantially, as it comes down to an additional term in the denominator of eq. (99), and the calculations for the reconstruction will happen in the Fourier domain anyways. Finally, σ can typically be determined from information on the noise level and the regularisation parameters

τ_1 and τ_2 can be chosen from the norm of the (initial) 3D map:

$$\sigma := \frac{1}{N} \sum_{i=1}^N \text{Var}(f_i) \quad \text{and} \quad \tau_1 := \tau_2 := \|u^0\|_2^2, \quad (100)$$

where $\text{Var}(f_i)$ is the variance of the pixel-values of the i :th image.

Remark 6.1. *We use lifting to re-phrase the non-convex optimisation problem for estimating particle-specific 3D rotations in Cryo-EM. This leads to algorithm 2 that is then tested on a realistic single particle Cryo-EM setting to evaluate its potential for incorporation in similar joint refinement schemes. In other words, in this work we do not intend to propose a state-of-the-art joint estimation scheme with respect to the current 3D map update routine. As an example, joint schemes with more carefully chosen 3D map updates steps – like recent ones based on more sophisticated priors [25] – will most likely yield a better 3D map reconstruction. However, this is beyond the scope of this article.*

Algorithm 2 ESL-based joint 3D map reconstruction and rotation estimation

Initialisation: $\mathcal{X} \subset \text{SO}(3)$, $u^0 \in L^2(\Omega)$, $\sigma, \tau_1, \tau_2 > 0$, $J_0 \geq 1$, $\eta \in (\frac{1}{4}, \frac{2}{3})$

$k := 0$

$J := \left\lfloor J_0 |\mathcal{X}|^{\frac{2-3\eta}{5}} \right\rfloor$

while not converged **do**

Update rotations

$$\gamma_i^{k+1} := \frac{1}{2} J_0^{\frac{5}{3}} \left(\frac{|\mathcal{X}|}{J} \right)^{\frac{2}{3}} \left(\frac{1}{2\sigma} \|\mathcal{A}(g_{(J+1)}^k \cdot u^k) - f_i\|_2^2 - \frac{1}{J} \sum_{j=1}^J \frac{1}{2\sigma} \|\mathcal{A}(g_{(j)}^k \cdot u^k) - f_i\|_2^2 \right)$$

$$\beta_i^{k+1} := \prod_{\Delta|\mathcal{X}|} \left(-\frac{|\mathcal{X}|^\eta}{\gamma_i^{k+1}} \left(\frac{1}{2\sigma} \|\mathcal{A}(g \cdot u^k) - f_i\|_2^2 \right)_{g \in \mathcal{X}} \right) \quad \text{for } i = 1, \dots, N$$

$l := 0$

$$g_i^{k+1,0} := \underset{g \in \mathcal{X}}{\text{argmax}} (\beta_i^{k+1})_g \quad \text{for } i = 1, \dots, N$$

while not converged **do**

$$g_i^{k+1,l+1} := \exp_{g_i^{k+1,l}} \left(\sum_{g \in \mathcal{X}} (\beta_i^{k+1})_g \log_{g_i^{k+1,l}}(g) \right) \quad \text{for } i = 1, \dots, N$$

$l := l + 1$

end while

$$g_i^{k+1} := g_i^{k+1,l}$$

Update 3D map

$$u^{k+1} := a^{k+1} * \sum_{i=1}^N \frac{\tau_1}{\sigma} (g_i^{k+1})^{-1} \cdot \mathcal{A}^*(f_i) \quad \text{for } a^{k+1} \text{ from eq. (99)}$$

$k := k + 1$

end while

6.2 Noise-robust and data-consistent computationally feasible lifting

Joint recovery approaches, such as the one above, typically involve a trade-off between noise robustness and data consistency – in the sense that the algorithm is still solving eq. (94) – in order to remain computationally feasible. With computational feasibility as a basic requirement, prior works have arguably only managed to obtain either noise-robustness or data-consistency.

In the following we briefly argue that our method is *computationally feasible* and has the potential to accomplish *both noise-robustness and data-consistency* by comparing it to the algorithms that underlies two of the most widespread software packages for single particle Cryo-EM: RELION [57] and cryoSPARC [54].

Computational feasibility The 3D map reconstruction scheme should be able to perform similarly to schemes in the aforementioned software packages, the potential bottleneck being the estimation of the particle-specific 3D rotations.

The computationally costly part of the rotation estimation lies in evaluating the objective function eq. (95) for all 3D rotations in \mathcal{X} . Indeed, once that is done, projecting onto the simplex is cheap and computing the Riemannian barycentre of a few points per image can be done very quickly. Similar to RELION, the proposed lifting scheme requires evaluating $|\mathcal{X}|$ rotations at each iteration. Although, the TEM simulations (projections) $(\mathcal{A}(g, u^k))_{g \in \mathcal{X}}$ can be reused for all the images, the method will be more costly than cryoSPARC, which needs much fewer function evaluations for its branch-and-bound scheme.

In practice, as we shall see in section 7, the proposed lifting scheme can potentially get closer to the correct rotations than RELION can with the same amount of sampling points, because of the additional step of computing the Riemannian barycentre. This suggests that the proposed method could be made faster than RELION – without loss of accuracy – and bring the method in the ballpark of cryoSPARC.

Noise-robustness In Cryo-EM, estimation of particle-specific 3D rotations is not only the challenging part because of the non-convexity, but also because of the high noise level in the data. As noise increases, we know that with inverse problems one should be careful when minimising eq. (95) without regularisation. RELION introduces resilience against such noise by marginalising over 3D rotations, i.e., by averaging over possible rotations for each particle. In contrast, cryoSPARC does not attempt to introduce a specific technique for resilience against noise in their branch-and-bound approach.

Our proposed method is arguably more similar to RELION concerning noise robustness. For that, note that evaluating any function at the Riemannian barycentre of a probability measure is actually similar to integrating the function over this measure, as the latter bounds the former in the weak topology (lemma 4.4). In other words, using the barycentre of a weighted set of points rather than taking the RELION approach of considering *all* the points in the 3D map reconstruction will yield similar outcomes as long as the support of the measure is local and noise-robustness is inherited from the averaging step.

Data-consistency Finally, the way orientations are optimised over hugely impacts the data-consistency. In the case of RELION we are no longer solving eq. (94) because of the introduced averaging over the space of orientations. Then when updating the 3D map, RELION is not using just 1 orientation per image, but uses multiple with different weights, which can smudge the obtained 3D map. In other words, lack of consistency with eq. (94) can impact the angular resolution of the method.

Note that cryoSPARC does not have this issue, as at the end of the orientation estimation part there is just one orientation per image. So as long as the orientation estimation has not suffered too much under the noise this method is likely to give higher resolution images than RELION. The lifting-based approach is more like cryoSPARC in this aspect.

7 Numerical experiments

Through Cryo-EM data we aim to test the validity of the theoretical results on the sparsity of the minimizer and on the error bounds (theorems 3.6 and 3.7) and test the performance of ESL (algorithm 1) as a global optimisation method and its potential when included in a joint recovery method (algorithm 2). Additionally, the practical use of proposition 3.8 will be considered.

Dataset The algorithms will be tested on a synthetic single particle Cryo-EM dataset of the spike protein of the SARS-CoV-2 (Delta variant). Using Chimera [52], a ground-truth 3D map u^{GT} (fig. 2a) is generated on a $91 \times 91 \times 91$ grid with a voxel size of 0.21667 nm. This 3D map is also used to generate $N = 2048$ 2D TEM image patches (projection images) $(f_i)_{i=1}^N$ of size 91×91 (fig. 2c). These image patches are generated by first randomly rotating the 3D map using rotations $(g_i^{\text{GT}})_{i=1}^N$ that are uniformly distributed over $\text{SO}(3)$, then applying the TEM forward operator eq. (88) as implemented in ASPIRE¹. The forward operator is parametrized by the electron wavenumber $k = 0.25 \text{ nm}^{-1}$, which corresponds to the (relativistically corrected) wavelength of a 200 kV electron. The TEM optics model has defocus $\Delta z = 1.5 \text{ }\mu\text{m}$ and spherical aberration $C_s = 2 \text{ mm}$. Furthermore, the amplitude contrast is set to $\alpha = 0.1$. These parameters are chosen to mimic a realistic setting (cf. [57, Table 2]). Additionally, the low-pass filter $A(\xi)$ in the CTF is omitted. For each TEM projection image, noise is added corresponding to a noise level where signal-to-noise-ratio (SNR) is 1/16. Finally, The ground true 3D map is also blurred by convolving against a normalized Gaussian kernel with standard deviation 10 to get a realistic initial density u^{INIT} (fig. 2b).

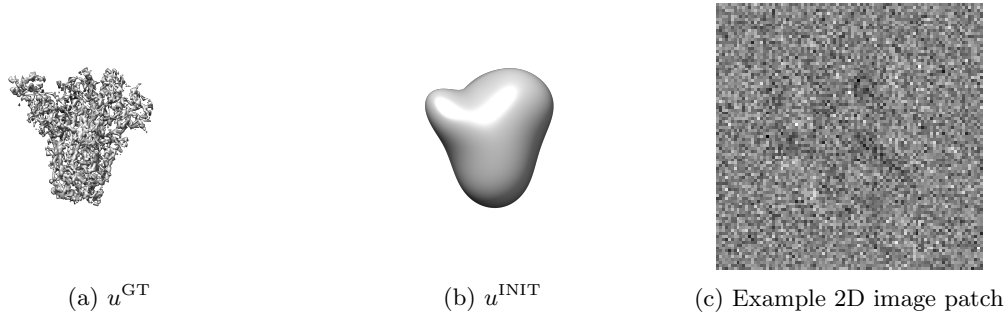


Figure 2: Synthetic dataset generated from the delta variant of the SARS-CoV-2 spike protein.

Overview of Experiments Theorems 3.6 and 3.7 and algorithm 1 are tested through orientation estimation of the 3D map u^{GT} for all N 2D TEM image patches (section 7.1) using a fixed regularisation parameter γ , but with varying sizes of sampling sets \mathcal{X} and varying values for the scaling parameter η . Because of the high resolution of u^{GT} , the optimisation landscape

¹<http://spr.math.princeton.edu/>

over $\text{SO}(3)$ will be rougher than when starting from a lower-resolution (initial) volume. The main reason here is to give an indication of the performance of algorithm 1 on a challenging problem rather than a toy example. Additionally, while testing scaling of errors for different \mathcal{X} and η , we implicitly test whether the orientation finding algorithm is able to perform well in a late stage of a joint recovery algorithm, e.g., algorithm 2.

Once some best practices have been gathered, it is time to check the performance of algorithm 1 in an iterative fashion through algorithm 2 and investigate whether one can control the amount of points in the sampling set through proposition 3.8 in a realistic setting (section 7.2).

Cryo-EM-related considerations For evaluating rotations one should consider that the joint 3D map reconstruction and orientation estimation problem can be solved up to a global rotation or reflection. Hence, any obtained rotation will be aligned with the ground truth rotations through finding a minimal orthogonal transformation as done in [63, (5.1)]. Then, after alignment, we use the distance in the $\text{SO}(3)$ metric and related distance measures, e.g., the Wasserstein-2 distance to compare rotations $(g_i)_{i=1}^N$ against the ground truth, i.e., $d_{\text{SO}(3)}(g_i, g_i^{\text{GT}})$. Note that, in general, the ground truth rotation does not have to coincide with any minimiser of the orientation estimation problem – however one expects that these coincide fairly well.

7.1 Scaling of the error rates

The performance of ESL (algorithm 1) and the validity of the theoretical results theorems 3.6 and 3.7 are tested for a fixed γ and varying \mathcal{X} and η through running one rotation update step of algorithm 2. More precisely, for fixed γ – possibly parametrized by J_0 as suggested in eq. (19) – the sampling set \mathcal{X} and the scaling parameter η are the relevant factors in the theoretical bounds.

We know from section 6.1 that fixing γ is by no means restrictive as the effect of γ can be compensated for by η and vice versa. Indeed, either could be varied while the other is fixed to establish any weight for the Tikhonov regulariser in eq. (13). In other words, the effect of larger γ on the amount of points with non-zero coefficients – or equivalently the effect of J_0 – can also be studied by varying η .

Two main questions follow naturally:

1. Is computing the Riemannian barycentre from the obtained weights actually beneficial in practice compared to just picking the rotation with minimal cost?
2. Do the theoretical bounds on (a) the algorithm’s number of non-zero coefficients and (b) the error hold in practice?

Additionally, in practice there is an argument to make to pick η as large as possible. Theorem 3.6 suggests that for $\eta \approx \frac{2}{3}$ and as long as the quality of the sampling set admits it, the amount of points with non-zero coefficients can be controlled more precisely as the upper and lower bound hardly vary for larger \mathcal{X} . Again, because the effect of η can be compensated by γ – as mentioned above – it then remains to pick the latter properly. Two additional questions follow:

3. Can we pick $\eta \approx \frac{2}{3}$, i.e., does the sampling set generating procedure described in section 6 satisfy the technical condition underlying the main theoretical results?
4. How to pick γ – or how to choose J_0 ?

Metrics Besides the average of the distances $d_{\text{SO}(3)}(g_i^1, g_i^{\text{GT}})$, where g_i^1 is the rotation obtained from the update scheme, several additional metrics will be considered for each \mathcal{X} and each η to investigate the first two questions.

1. For testing algorithm 1: the average of the distances $d_{\text{SO}(3)}(g_i^{1,0}, g_i^{\text{GT}})$ of the rotation with largest coefficient, i.e., the initialisation of Riemannian gradient descent $g_i^{1,0}$, will be considered.
2. (a) For testing theorem 3.6: the average of the ℓ^0 -norms $\|\beta_i^1\|_0$.
(b) For testing theorem 3.7: the average of the Wasserstein-2 distances $W_2(\mu_i^1, \delta_{g_i^{\text{GT}}})$ of the measure $\mu_i^1 := \sum_{g \in \mathcal{X}} (\beta_i^1)_g \delta_g$ to the Dirac measure concentrated on the ground truth, will be considered, because this is the main ingredient for the scaling behaviour.

As we shall see, the latter two questions will follow from these metrics.

Algorithm settings We use $u^0 := u^{\text{GT}}$, σ as in eq. (100) and $\gamma := 30$. Here the latter is chosen large enough such that the lifting scheme does not collapse into a single rotation. For computing the Riemannian barycentre, 20 descent steps are taken.

Three sampling sets and six scaling parameters will be considered. The three sampling sets \mathcal{X}_1 , \mathcal{X}_2 and \mathcal{X}_3 are generated from iterative midpoint refinement of the sampling set \mathcal{X}_0 with $|\mathcal{X}_0| = 1821$ as mentioned in section 6. We have $|\mathcal{X}_1| = 14761$, $|\mathcal{X}_2| = 114564$ and $|\mathcal{X}_3| = 860069$. The scaling factors are chosen as $\eta \in \{0.26, 0.3, 0.4, 0.5, 0.6, 0.66\}$, so that the whole feasible range $(\frac{1}{4}, \frac{2}{3})$ is taken into account.

Riemannian barycentre vs. minimal cost rotation Regarding question 1, we computed averages of the distances $d_{\text{SO}(3)}(g_i^{1,0}, g_i^{\text{GT}})$ and $d_{\text{SO}(3)}(g_i^1, g_i^{\text{GT}})$. The results in tables 1 and 2 indicate that averaging using algorithm 1 performs better by a factor of 2 compared to picking the rotation with maximal weight, for which one normally needs about 8 times as many points on $\text{SO}(3)$ to obtain the same accuracy.

Table 1: Distance $d_{\text{SO}(3)}(g_i^{1,0}, g_i^{\text{GT}})$ of the rotation with minimal cost to the ground truth for different sizes of sampling set \mathcal{X} (baseline). Numbers are reported in degrees and averaged over all rotations.

$ \mathcal{X} $	$d_{\text{SO}(3)}(g_{\mathcal{X}}^0, g^*)$ ($^\circ$)
14 761	5.026 ± 1.727
114 564	2.758 ± 0.948
860 069	1.541 ± 0.605

Bounding the number of non-zero coefficients For part (a) of question 2, the average number of points with non-zero coefficients, i.e., $\|\beta_i^1\|_0$, used to compute the Riemannian barycentres is provided in table 3. From the results in table 3 it is not directly clear whether the scaling behaviour predicted by theorem 3.6 holds. As $\|\beta_i^1\|_0$ does not scale as predicted, but rather decreases with $|\mathcal{X}|$ for all instances of η , one would say that either there are not enough points for the scaling to kick in or the technical condition has not been satisfied.

However, we would argue that the theoretical result is likely to hold. That is, the predicted range is fairly broad so one should be careful immediately comparing between different sampling sets. A better indication of the validity of the scaling is to compare the ratio of upper bounds between different η -values with the ratio of the observed number of points for a given sampling

Table 2: Distance $d_{\text{SO}(3)}(g_i^1, g_i^{\text{GT}})$ of the (Riemannian barycentre) rotation obtained by algorithm 1 to the ground truth for different sizes of sampling set \mathcal{X} and different choices of η (ours). Varying η while keeping $\gamma = 30$ fixed directly influences the number of non-zero coefficients in the solution. Numbers are again reported in degrees and averaged over all rotations. For properly chosen η , the method outperforms the baseline approach table 1 by approximately a factor of two (bold).

$ \mathcal{X} $	$\eta = 0.26$	$\eta = 0.3$	$\eta = 0.4$	$\eta = 0.5$	$\eta = 0.6$	$\eta = 0.66$
14 761	37.628 ± 16.024	32.005 ± 14.674	18.226 ± 10.407	7.116 ± 5.548	2.54 ± 1.821	2.026 ± 1.178
114 564	4.959 ± 4.154	2.953 ± 2.36	1.613 ± 0.845	1.229 ± 0.583	1.14 ± 0.534	1.2 ± 0.575
860 069	1.236 ± 0.588	1.108 ± 0.524	0.925 ± 0.428	0.858 ± 0.389	0.87 ± 0.406	0.938 ± 0.446

set. The ratios relative to $\eta = 0.66$ are provided in table 4 and show that for all values of η the empirical ratio gets closer to the predicted values for larger sampling sets, which is in line with theorem 3.6.

Table 3: The average number of points with non-zero coefficients, i.e., $\|\beta_i^1\|_0$, for different sizes of sampling set \mathcal{X} and different numbers of non-zero coefficients. Varying the latter is realized through a varying η , but fixed $\gamma = 30$. Bold values correspond to the value or η that gave minimal average error for each sampling set, cf. table 2. Without normalization – as done in table 4 – it is not immediately clear that the results are in line with theory for larger sampling sets.

$ \mathcal{X} $	$\eta = 0.26$	$\eta = 0.3$	$\eta = 0.4$	$\eta = 0.5$	$\eta = 0.6$	$\eta = 0.66$
14 761	760.77 ± 92.25	517.52 ± 68.78	173.46 ± 32.22	47.068 ± 10.762	16.167 ± 2.953	9.889 ± 1.863
114 564	253.32 ± 51.7	151.67 ± 25.39	55.684 ± 7.449	22.732 ± 3.356	9.655 ± 1.916	5.948 ± 1.413
860 069	204.95 ± 25.76	135.53 ± 17.07	49.646 ± 6.585	19.032 ± 3.031	7.847 ± 1.771	4.721 ± 1.339

Table 4: A comparison of theoretical and empirical ratios of average number of points with non-zero coefficients from the results in table 3. For larger sampling sets the discrepancy between theory and practice closes in.

$ \mathcal{X} $	$\frac{\ \beta_i^*\ _0 _{\eta=(\cdot)}}{\ \beta^*\ _0 _{\eta=0.66}}$	$\eta = 0.26$	$\eta = 0.3$	$\eta = 0.4$	$\eta = 0.5$	$\eta = 0.6$
14 761	predicted	10.014	7.953	4.471	2.513	1.413
	observed	76.931	52.333	17.541	4.76	1.635
114 564	predicted	16.375	12.381	6.155	3.06	1.521
	observed	42.589	25.499	9.362	3.822	1.623
860 069	predicted	26.564	19.136	8.429	3.713	1.635
	observed	43.412	28.708	10.516	4.031	1.662

Bounding the error For the part (b) of question 2, getting back to table 2, again it is not directly clear whether or not the scaling behaviour of the error bound in theorem 3.7 holds. The scaling seemingly fails as values for η yielding more points with non-zero coefficients obtain a lower average error for larger sampling sets (bold numbers in table 2).

However, this effect is arguably due to the observation in remark 4.5, where we already mentioned that the bound in theorem 3.7 itself relies upon the scaling of the Wasserstein-2 distances, which are provided in table 5, that does not take the averaging effect of using more points with non-zero coefficient into account. The Wasserstein-2 distance – or rather twice the value – does bound the error, i.e., table 2 is entry-wise smaller than table 5, and the scaling of

the errors in table 2 will still be in line with theory if the scaling of the Wasserstein-2 distances in table 5 is in line with theory. In other words, we should test our theoretical prediction on the scaling of the error for the Wasserstein-2 distance. Similarly to the number of non-zero coefficients it is not obvious whether or not the scaling behaviour is kicking in. Comparing ratios – similarly as before – we observe in table 6 again that theory and empirical results agree better for larger sampling sets. Overall, this experiment is in line with theorem 3.7, but the derived bound is overly pessimistic – as predicted in remark 4.5 – in the sense that there is a discrepancy between the errors in table 2 and the Wasserstein-2 errors in table 5 that the theory does not account for.

Table 5: The average of the distances $W_2(\sum_{g \in \mathcal{X}} (\beta_i^1)_g \delta_g, \delta_{g_{\text{GT}}})$ in degrees ($^\circ$) for different sizes of sampling set \mathcal{X} and different numbers of non-zero coefficients, where the latter is realized through a varying η , but fixed $\gamma = 30$. Bold values correspond to the value or η that gave minimal average error for each sampling set, cf. table 2. Without normalization – as done in table 6 – it is not immediately clear that the results are in line with theory for larger sampling sets.

$ \mathcal{X} $	$\eta = 0.26$	$\eta = 0.3$	$\eta = 0.4$	$\eta = 0.5$	$\eta = 0.6$	$\eta = 0.66$
14 761	108.68 \pm 7.196	101.495 \pm 8.781	74.179 \pm 13.95	34.403 \pm 14.731	12.283 \pm 4.68	9.481 \pm 2.439
114 564	24.769 \pm 12.06	14.76 \pm 6.628	8.44 \pm 1.524	6.175 \pm 0.559	4.66 \pm 0.508	3.984 \pm 0.538
860 069	6.58 \pm 0.589	5.731 \pm 0.489	4.129 \pm 0.378	3.049 \pm 0.33	2.318 \pm 0.339	1.998 \pm 0.387

Table 6: A comparison of theoretical and empirical ratios of Wasserstein-2 distances from the results in table 5. For larger sampling sets the discrepancy between theory and practice closes in.

$ \mathcal{X} $	$\frac{W_2(\mu_{\mathcal{X}}^*, \delta_{g^*}) _{\eta=(\cdot)}}{W_2(\mu_{\mathcal{X}}^*, \delta_{g^*}) _{\eta=0.66}}$	$\eta = 0.26$	$\eta = 0.3$	$\eta = 0.4$	$\eta = 0.5$	$\eta = 0.6$
14 761	predicted	2.155	1.996	1.647	1.36	1.122
	observed	11.463	10.705	7.824	3.629	1.296
114 564	predicted	2.539	2.313	1.833	1.452	1.15
	observed	6.217	3.705	2.118	1.55	1.17
860 069	predicted	2.984	2.675	2.035	1.548	1.178
	observed	3.293	2.868	2.067	1.526	1.16

Choosing the parameter η For question 3, it is currently unknown whether our choice of sampling sets fulfills the technical condition of η -local low-discrepancy with $\eta \approx 2/3$. However, empirical evidence of the scaling behaviour (tables 4 and 6) suggests that this choice is justified for the two largest sampling sets.

Choosing regularization strength Finally, for question 4, choosing the regularisation parameter γ , tables 2 and 3 suggest that there is a sweet spot for the number of non-zero coefficients and the regularisation parameter γ , i.e., the bold numbers in the tables suggest that the number of non-zero coefficients should not be chosen as small as possible but not too large either and this should be reflected in the choice of γ .

Best practices Overall, the results from this experiment lead to the following best practice for the current dataset:

1. Use a sufficiently large sampling set, e.g., \mathcal{X}_2 ,

2. pick η as large as possible $\eta \approx 2/3$, and
3. choose γ yielding a proper amount of points with non-zero coefficient, e.g., having \mathcal{X}_2 where $\|\beta_i^1\|_0$ is between 7 and 20 on average.

The latter will be achieved through a proper choice of J_0 and the use of proposition 3.8 in the following section.

7.2 Joint 3D map reconstruction and rotation estimation

In this experiment we will test the performance of ESL (algorithm 1) in the alternating minimisation scheme in algorithm 2 and see to what extend proposition 3.8 allows us to pick the amount of non-zero coefficients. We will be concerned with more straightforward questions than the ones in the previous section:

1. Does lifting-based orientation estimation perform well in a joint scheme with 3D map reconstruction?
2. Can theory help controlling the number of non-zero coefficients?

Metrics The following metrics will be used to investigate the questions above.

1. For testing algorithm 2: the progression of the distribution of $d_{\text{SO}(3)}(g_i^k, g_i^{\text{GT}})$.
2. For testing proposition 3.8: the progression of the distribution of $\|\beta_i^k\|_0$.

For the sake of completeness, a progression of the 3D maps will also be provided for visual inspection.

Algorithm settings We use $\mathcal{X} := \mathcal{X}_2$ from the previous experiment, $u^0 := u^{\text{INIT}}$, σ, τ_1, τ_2 as in eq. (100), $J_0 = 15$ and $\eta = 0.66$. In total, 10 iterations of algorithm 2 will be done with 20 Riemannian gradient descent iterations in the inner loop.

Results The progression of the distribution of errors, the amount of non-zero coefficients and the 3D map are shown in fig. 3 for iterations 1, 5, and 10.

For question 1, for all the images the distance between the estimated rotation to the ground truth decreases. After 10 iterations the average distance is 1.417 ± 0.685 , which is slightly worse than the results obtained in the previous experiment. This is no surprise as the 3D map u^k has less detail than the ground truth, which makes it arguably harder to get high angular accuracy. Overall, the lifting-based orientation estimation scheme performs well in the joint scheme.

Regarding question 2, according to theory the amount of non-zero coefficients should lie between 8 and 15. From the figure we observe that the upper bound is satisfied at all times, but that the lower bound is violated at all the iterates. The latter is most likely due to the size of the sampling set. Overall, the results are reasonably in line with theory and from a practical point of view proposition 3.8 has delivered.

Finally, it should be mentioned that the resolution of the obtained 3D maps after 10 iterations is visibly lower than the ground truth. The reason is twofold. First, with the small data size we cannot expect very high resolution, but – more importantly – in real-life data, a defocus depth *range* is used rather than a single defocus depth. This is an important detail as this prevents losing certain frequency bands in Fourier space on the zero-crossings of the CTF. However, we remind the reader that this work focuses on orientation estimation and that such considerations are beyond the scope of this work.

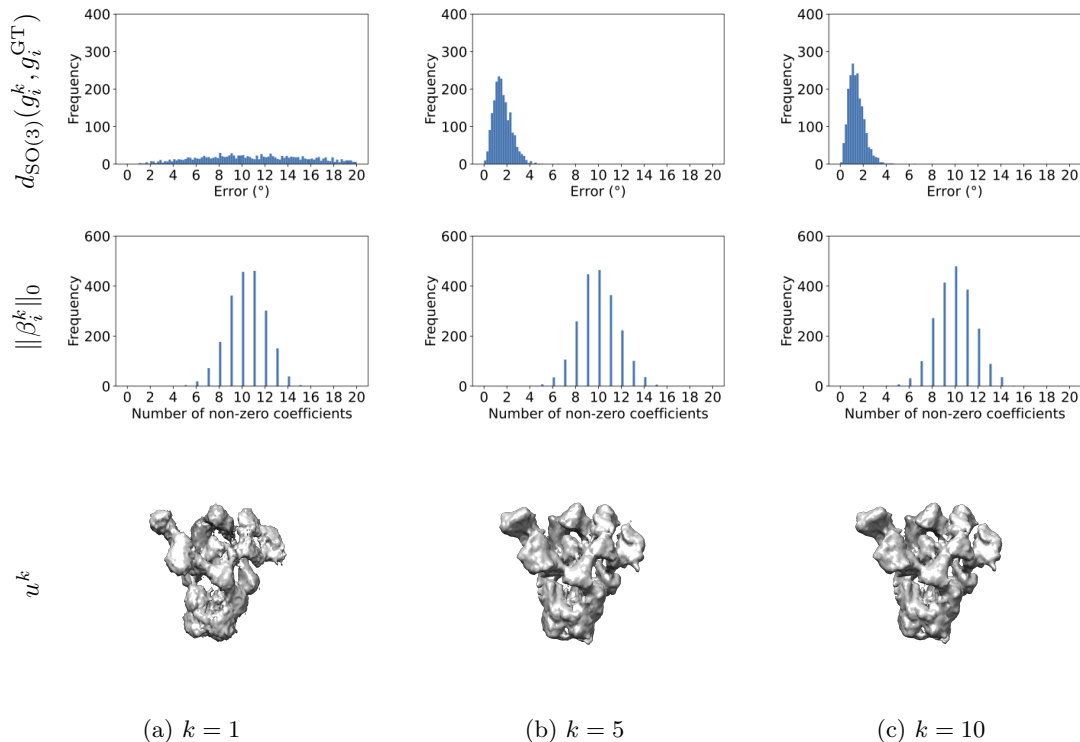


Figure 3: The progression of the distribution of the rotation estimation error, the number of non-zero coefficients and the 3D map. The orientation estimation scheme has more or less converged after 5 iterations and the number of non-zero coefficients are in line with the theory.

8 Conclusions

In this work we presented ellipsoidal support lifting (ESL) as a general lifting-based algorithm for approximating the global minimiser of a smooth function over a Riemannian manifold. The main theoretical result is that the algorithm is well-posed; we also provided upper bounds on the distance to the minimiser. Additionally, several minor results were provided that can be used to make the algorithm more practically useful.

These theoretical results have been tested in several numerical experiments related to single particle Cryo-EM. Not only do these experiments support the theory, they also showcase the practical usefulness of ESL. That is, in the Cryo-EM test case ESL needs eight times less rotations in the sampling set to get the same error as when picking the rotation with minimal cost, which has a huge impact on the time it takes to update the rotations.

Besides promising numerical performance we have argued – in a more heuristic fashion – that ESL in a joint refinement scheme could yield a data-consistent and noise-robust rotation estimation – contrary to popular methods such as CryoSPARC and RELION, which have arguably only managed to tackle either data-consistency or noise-robustness. To the best of our knowledge, this work is the first attempt to design an algorithm that aims to tackle both these issues. However, a fair comparison of the three methods to test this hypothesis on several data sets is left for future research as it is beyond the scope of this work.

Finally, we see further potential of the proposed theory in the context of single particle

Cryo-EM as follows:

Symmetric molecules Symmetries do not pose an issue in our framework regarding non-uniqueness of minimisers, the reason being that such symmetries can be quotiented out and our results still hold on the quotient manifold. As an example, assume the molecule 3D map u has a rotation symmetry generated by some finite subgroup $G \subset \text{SO}(3)$. We can then consider the manifold $\text{SO}(3)/G$ and adapt algorithm 2 for solving

$$\inf_{\substack{u \in L^2(\Omega) \\ g_i \in \text{SO}(3)/G}} \left\{ \sum_{i=1}^N \left[\frac{1}{|G|} \sum_{g \in G} \frac{1}{2\sigma} \|\mathcal{A}((g \circ g_i).u) - f_i\|_2^2 \right] + \mathcal{R}(u) \right\} \quad \text{for } \sigma > 0. \quad (101)$$

Additionally, our theoretical bounds suggest that in the case of $|G|$ -fold symmetry we would only need $1/|G|$ times the amount of rotations in the sampling set \mathcal{X} to get the same error bound as for a non-symmetric molecule.

In-plane shifts In experimental 3D map and orientation reconstruction, one also considers 2D in-plane shifts of the molecule due to improper alignment of the particles, i.e., the actual manifold of interest is a bounded subset of $\text{SO}(3) \times \mathbb{R}^2$. Algorithm 2 does not change except that our theoretical results suggest that one should choose $\eta \in (\frac{1}{6}, \frac{2}{5})$ since the manifold $\text{SO}(3) \times \mathbb{R}^2$ is now five-dimensional.

Local search The theory suggests that instead of increasing the amount of points in the sampling set it can be equally efficient to reduce the volume of the manifold, i.e., the search area. This is already done in RELION as a local search and in cryoSPARC through the multi-scale nature of branch-and-bound. Our framework would also be suitable here as bounded sub-manifolds satisfy the conditions for the theory to hold.

Acknowledgments

We would like to thank Sjors Scheres, Dari Kimanius and Johannes Schwab for fruitful discussions throughout this project.

References

- [1] P-A Absil, Robert Mahony, and Rodolphe Sepulchre. Optimization algorithms on matrix manifolds. In *Optimization Algorithms on Matrix Manifolds*. Princeton University Press, 2009.
- [2] Miroslav Bacák. Computing medians and means in hadamard spaces. *SIAM journal on optimization*, 24(3):1542–1566, 2014.
- [3] Afonso S Bandeira, Ben Blum-Smith, Joe Kileel, Amelia Perry, Jonathan Weed, and Alexander S Wein. Estimation under group actions: recovering orbits from invariants. *arXiv preprint arXiv:1712.10163*, 2017.
- [4] Afonso S Bandeira, Yutong Chen, Roy R Lederman, and Amit Singer. Non-unique games over compact groups and orientation estimation in cryo-em. *Inverse Problems*, 36(6):064002, 2020.

- [5] Sebastian Banert. Backward-backward splitting in hadamard spaces. *Journal of Mathematical Analysis and Applications*, 414(2):656–665, 2014.
- [6] Samit Basu and Yoram Bresler. Feasibility of tomography with unknown view angles. *IEEE Transactions on Image Processing*, 9(6):1107–1122, 2000.
- [7] Samit Basu and Yoram Bresler. Uniqueness of tomography with unknown view angles. *IEEE Transactions on Image Processing*, 9(6):1094–1106, 2000.
- [8] Tamir Bendory, Alberto Bartesaghi, and Amit Singer. Single-particle cryo-electron microscopy: Mathematical theory, computational challenges, and opportunities. *IEEE Signal Processing Magazine*, 37(2):58–76, 2020.
- [9] Ronny Bergmann, Raymond H Chan, Ralf Hielscher, Johannes Persch, and Gabriele Steidl. Restoration of manifold-valued images by half-quadratic minimization. *arXiv preprint arXiv:1505.07029*, 2015.
- [10] Ronny Bergmann, Roland Herzog, Maurício Silva Louzeiro, Daniel Tenbrinck, and José Vidal-Núñez. Fenchel duality theory and a primal-dual algorithm on riemannian manifolds. *Foundations of Computational Mathematics*, 21(6):1465–1504, 2021.
- [11] Ronny Bergmann, Friederike Laus, Johannes Persch, and Gabriele Steidl. Recent advances in denoising of manifold-valued images. *Handbook of Numerical Analysis*, 20:553–578, 2019.
- [12] Ronny Bergmann, Johannes Persch, and Gabriele Steidl. A parallel douglas-rachford algorithm for minimizing rof-like functionals on images with values in symmetric hadamard manifolds. *SIAM Journal on Imaging Sciences*, 9(3):901–937, 2016.
- [13] Tejal Bhamre, Teng Zhang, and Amit Singer. Orthogonal matrix retrieval in cryo-electron microscopy. In *2015 IEEE 12th International Symposium on Biomedical Imaging (ISBI)*, pages 1048–1052. IEEE, 2015.
- [14] William M Boothby and William Munger Boothby. *An introduction to differentiable manifolds and Riemannian geometry, Revised*, volume 120. Gulf Professional Publishing, 2003.
- [15] Nicolas Boumal. An introduction to optimization on smooth manifolds. *Available online*, Aug, 2020.
- [16] G. Bouvier, B. Bardiaux, R. Pellarin, C. Rapisarda, and M. Nilges. Automatic building of protein atomic models from cryo-EM density maps using residue co-evolution. *bioRxiv*, 2020.
- [17] Luca Brandolini, Christine Choirat, Leonardo Colzani, Giacomo Gigante, Raffaello Seri, and Giancarlo Travaglini. Quadrature rules and distribution of points on manifolds. *arXiv preprint arXiv:1012.5409*, 2010.
- [18] Manfredo Perdigao do Carmo. *Riemannian geometry*. Birkhäuser, 1992.
- [19] Lenaic Chizat. Sparse optimization on measures with over-parameterized gradient descent. *Mathematical Programming*, pages 1–46, 2021.
- [20] Willem Diepeveen and Jan Lellmann. An inexact semismooth newton method on riemannian manifolds with application to duality-based total variation denoising. *SIAM Journal on Imaging Sciences*, 14(4):1565–1600, 2021.

- [21] J. Duchi, S. Shalev-Shwartz, Y. Singer, and T. Chandra. Efficient projections onto the ℓ_1 -ball for learning in high dimensions. In *Proceedings of the 25th International Conference on Machine Learning (ICML 2008), Helsinki, Finland, 2008*.
- [22] Massimo Fornasier, Hui Huang, Lorenzo Pareschi, and Philippe Sünnen. Consensus-based optimization on hypersurfaces: Well-posedness and mean-field limit. *Mathematical Models and Methods in Applied Sciences*, 30(14):2725–2751, 2020.
- [23] Joachim Frank, Michael Radermacher, Pawel Penczek, Jun Zhu, Yanhong Li, Mahieddine Ladjadj, and Ardean Leith. Spider and web: processing and visualization of images in 3d electron microscopy and related fields. *Journal of structural biology*, 116(1):190–199, 1996.
- [24] Peter Gilbert. Iterative methods for the three-dimensional reconstruction of an object from projections. *Journal of theoretical biology*, 36(1):105–117, 1972.
- [25] Marc Aurèle Gilles and Amit Singer. A molecular prior distribution for bayesian inference based on wilson statistics. *arXiv preprint arXiv:2202.09388*, 2022.
- [26] AB Goncharov. Methods of integral geometry and finding the relative orientation of identical particles arbitrarily arranged in a plane from their projections onto a straight line. *SPhD*, 32:177, 1987.
- [27] AB Goncharov. Integral geometry and three-dimensional reconstruction of randomly oriented identical particles from their electron microphotos. *Acta Applicandae Mathematica*, 11(3):199–211, 1988.
- [28] AB Goncharov and MS Gelfand. Determination of mutual orientation of identical particles from their projections by the moments method. *Ultramicroscopy*, 25(4):317–327, 1988.
- [29] Manuel Gräf. A unified approach to scattered data approximation on s^3 and so (3). *Advances in Computational Mathematics*, 37(3):379–392, 2012.
- [30] Manuel Gräf and Daniel Potts. Sampling sets and quadrature formulae on the rotation group. *Numerical Functional Analysis and Optimization*, 30(7-8):665–688, 2009.
- [31] Nikolaus Grigorieff. Frealign: high-resolution refinement of single particle structures. *Journal of structural biology*, 157(1):117–125, 2007.
- [32] Philipp Grohs and Seyedehsomyeh Hosseini. Nonsmooth trust region algorithms for locally lipschitz functions on riemannian manifolds. *IMA Journal of Numerical Analysis*, 36(3):1167–1192, 2016.
- [33] Harshit Gupta, Michael T McCann, Laurene Donati, and Michael Unser. Cryogan: a new reconstruction paradigm for single-particle cryo-em via deep adversarial learning. *IEEE Transactions on Computational Imaging*, 7:759–774, 2021.
- [34] George Harauz and FP Ottensmeyer. Direct three-dimensional reconstruction for macromolecular complexes from electron micrographs. *Ultramicroscopy*, 12(4):309–319, 1983.
- [35] Michael Hohn, Grant Tang, Grant Goodyear, Philip R Baldwin, Zhong Huang, Pawel A Penczek, Chao Yang, Robert M Glaeser, Paul D Adams, and Steven J Ludtke. Sparx, a new environment for cryo-em image processing. *Journal of structural biology*, 157(1):47–55, 2007.

- [36] Wen Jiang and Liang Tang. Atomic cryo-em structures of viruses. *Current opinion in structural biology*, 46:122–129, 2017.
- [37] Zvi Kam. The reconstruction of structure from electron micrographs of randomly oriented particles. *Journal of Theoretical Biology*, 82(1):15–39, 1980.
- [38] Hermann Karcher. Riemannian center of mass and mollifier smoothing. *Communications on pure and applied mathematics*, 30(5):509–541, 1977.
- [39] Wilfrid S Kendall. Probability, convexity, and harmonic maps with small image i: uniqueness and fine existence. *Proceedings of the London Mathematical Society*, 3(2):371–406, 1990.
- [40] Young-Heon Kim and Brendan Pass. Wasserstein barycenters over riemannian manifolds. *Advances in Mathematics*, 307:640–683, 2017.
- [41] Pär Kurlberg and Gustav Zickert. Formal uniqueness in Ewald sphere corrected single particle analysis. *arXiv preprint*, 2104.05371, 2021.
- [42] Lars Lamberg. Unique recovery of unknown projection orientations in three-dimensional tomography. *Inverse Problems & Imaging*, 2(4):547, 2008.
- [43] Thibaut Le Gouic and Jean-Michel Loubes. Existence and consistency of wasserstein barycenters. *Probability Theory and Related Fields*, 168(3):901–917, 2017.
- [44] John M Lee. Smooth manifolds. In *Introduction to Smooth Manifolds*, pages 1–31. Springer, 2013.
- [45] Jan Lellmann, Evgeny Strekalovskiy, Sabrina Koetter, and Daniel Cremers. Total variation regularization for functions with values in a manifold. In *Proceedings of the IEEE International Conference on Computer Vision*, pages 2944–2951, 2013.
- [46] Eitan Levin, Tamir Bendory, Nicolas Boumal, Joe Kileel, and Amit Singer. 3d ab initio modeling in cryo-em by autocorrelation analysis. In *2018 IEEE 15th International Symposium on Biomedical Imaging (ISBI 2018)*, pages 1569–1573. IEEE, 2018.
- [47] Steven J Ludtke, Philip R Baldwin, and Wah Chiu. Eman: semiautomated software for high-resolution single-particle reconstructions. *Journal of structural biology*, 128(1):82–97, 1999.
- [48] David G Luenberger. The gradient projection method along geodesics. *Management Science*, 18(11):620–631, 1972.
- [49] T. Nakane, A. Kotecha, A. Sente, G. McMullan, S. Masiulis, P. M. G. E. Brown, I. T. Grigoras, L. Malinauskaite, T. Malinauskas, J. Miehling, T. Uchański, L. Yu, D. Karia, E. V. Pechnikova, E. de Jong, J. Keizer, M. Bischoff, J. McCormack, P. Tiemeijer, S. W. Hardwick, D. Y. Chirgadze, G. Murshudov, R. A. Aricescu, and S. H. W. Scheres. Single-particle cryo-EM at atomic resolution. *Nature*, 587:152–156, 2020.
- [50] Ozan Öktem. Mathematics of electron tomography. 2015.
- [51] Johannes Persch. *Optimization Methods for Manifold-Valued Image Processing*. PhD thesis, 2018.

- [52] Eric F Pettersen, Thomas D Goddard, Conrad C Huang, Gregory S Couch, Daniel M Greenblatt, Elaine C Meng, and Thomas E Ferrin. Ucsf chimera—a visualization system for exploratory research and analysis. *Journal of computational chemistry*, 25(13):1605–1612, 2004.
- [53] Thomas Pock, Daniel Cremers, Horst Bischof, and Antonin Chambolle. Global solutions of variational models with convex regularization. *SIAM Journal on Imaging Sciences*, 3(4):1122–1145, 2010.
- [54] Ali Punjani, John L Rubinstein, David J Fleet, and Marcus A Brubaker. cryosparc: algorithms for rapid unsupervised cryo-em structure determination. *Nature methods*, 14(3):290–296, 2017.
- [55] Takashi Sakai. *Riemannian geometry*, volume 149. American Mathematical Soc., 1996.
- [56] David B Salzman. A method of general moments for orienting 2d projections of unknown 3d objects. *Computer vision, graphics, and image processing*, 50(2):129–156, 1990.
- [57] Sjors HW Scheres. Relion: implementation of a bayesian approach to cryo-em structure determination. *Journal of structural biology*, 180(3):519–530, 2012.
- [58] Tanvir R Shaikh, Haixiao Gao, William T Baxter, Francisco J Asturias, Nicolas Boisset, Ardean Leith, and Joachim Frank. Spider image processing for single-particle reconstruction of biological macromolecules from electron micrographs. *Nature protocols*, 3(12):1941, 2008.
- [59] Nir Sharon, Joe Kileel, Yuehaw Khoo, Boris Landa, and Amit Singer. Method of moments for 3d single particle ab initio modeling with non-uniform distribution of viewing angles. *Inverse Problems*, 36(4):044003, 2020.
- [60] Yoel Shkolnisky and Amit Singer. Viewing direction estimation in cryo-em using synchronization. *SIAM journal on imaging sciences*, 5(3):1088–1110, 2012.
- [61] Amit Singer. Mathematics for cryo-electron microscopy. In *Proceedings of the International Congress of Mathematicians: Rio de Janeiro 2018*, pages 3995–4014. World Scientific, 2018.
- [62] Amit Singer, Ronald R Coifman, Fred J Sigworth, David W Chester, and Yoel Shkolnisky. Detecting consistent common lines in cryo-em by voting. *Journal of structural biology*, 169(3):312–322, 2010.
- [63] Amit Singer and Yoel Shkolnisky. Three-dimensional structure determination from common lines in cryo-em by eigenvectors and semidefinite programming. *SIAM journal on imaging sciences*, 4(2):543–572, 2011.
- [64] Steven T Smith. Optimization techniques on riemannian manifolds. *Fields institute communications*, 3(3):113–135, 1994.
- [65] COS Sorzano, Roberto Marabini, Javier Velázquez-Muriel, José Román Bilbao-Castro, Sjors HW Scheres, José M Carazo, and Alberto Pascual-Montano. Xmipp: a new generation of an open-source image processing package for electron microscopy. *Journal of structural biology*, 148(2):194–204, 2004.

- [66] Guang Tang, Liwei Peng, Philip R Baldwin, Deepinder S Mann, Wen Jiang, Ian Rees, and Steven J Ludtke. Eman2: an extensible image processing suite for electron microscopy. *Journal of structural biology*, 157(1):38–46, 2007.
- [67] Todor D Todorov. The optimal refinement strategy for 3-d simplicial meshes. *Computers & Mathematics with Applications*, 66(7):1272–1283, 2013.
- [68] Constantin Udriste. *Convex Functions and Optimization Methods on Riemannian Manifolds*, volume 297. Springer Science & Business Media, 1994.
- [69] B K Vainshtein and A B Goncharov. Determination of the spatial orientation of arbitrarily arranged identical particles of unknown structure from their projections. In *Dokl. Akad. Nauk SSSR*, volume 287, pages 1131–1134, 1986.
- [70] Marin van Heel, George Harauz, Elena V Orlova, Ralf Schmidt, and Michael Schatz. A new generation of the imagic image processing system. *Journal of structural biology*, 116(1):17–24, 1996.
- [71] Cédric Villani. *Optimal transport: old and new*, volume 338. Springer, 2009.
- [72] Thomas Vogt, Evgeny Strekalovskiy, Daniel Cremers, and Jan Lellmann. Lifting methods for manifold-valued variational problems. In *Handbook of Variational Methods for Nonlinear Geometric Data*, pages 95–119. Springer, 2020.
- [73] Thomas Goar Vogt. *Measure-valued Variational Models with Applications in Image Processing*. PhD thesis, Universität zu Lübeck, 2019.
- [74] Miloš Vulović, Lenard M Voortman, Lucas J van Vliet, and Bernd Rieger. When to use the projection assumption and the weak-phase object approximation in phase contrast cryo-em. *Ultramicroscopy*, 136:61–66, 2014.
- [75] Lanhui Wang, Amit Singer, and Zaiwen Wen. Orientation determination of cryo-em images using least unsquared deviations. *SIAM journal on imaging sciences*, 6(4):2450–2483, 2013.
- [76] Robert S Womersley. Efficient spherical designs with good geometric properties. In *Contemporary computational mathematics-A celebration of the 80th birthday of Ian Sloan*, pages 1243–1285. Springer, 2018.
- [77] Mona Zehni, Laurène Donati, Emmanuel Soubies, Zhizhen Zhao, and Michael Unser. Joint angular refinement and reconstruction for single-particle cryo-em. *IEEE Transactions on Image Processing*, 29:6151–6163, 2020.
- [78] Hongyi Zhang and Suvrit Sra. First-order methods for geodesically convex optimization. In *Conference on Learning Theory*, pages 1617–1638. PMLR, 2016.
- [79] Ellen D Zhong, Adam Lerer, Joseph H Davis, and Bonnie Berger. Cryodrgn2: Ab initio neural reconstruction of 3d protein structures from real cryo-em images. In *Proceedings of the IEEE/CVF International Conference on Computer Vision*, pages 4066–4075, 2021.